Hydrogen self-dynamics in diluted liquid mixtures with neon: An inelastic neutron scattering study

Daniele Colognesi,[1,*] Ubaldo Bafile,[1] Milva Celli,[1] Martin Neumann,[2] Eleonora Guarini,[3] and Manh Duc Le[4]

[1]*Consiglio Nazionale delle Ricerche, Istituto di Fisica Applicata "N. Carrara", via Madonna del Piano 10, I-50019 Sesto Fiorentino, Italy*

[2]*Fakultät für Physik der Universität Wien, Strudlhofgasse 4, A-1090 Wien, Austria*

[3]*Dipartimento di Fisica e Astronomia, Università di Firenze, via G. Sansone 1, I-50019 Sesto Fiorentino, Italy*

[4]*ISIS Neutron and Muon Source, Rutherford Appleton Laboratory, Science and Technology Facilities Council,
Harwell Oxford, Didcot OX11 0QX, United Kingdom*

We have measured the dynamic structure factor of liquid neon-hydrogen mixtures ($T = 30.1$ K) at two different H_2 concentration levels (namely, 3.4% and 10%) making use of inelastic neutron scattering. This system has been selected since the presence of heavy Ne atoms strongly influences the self-dynamics of the H_2 centers of mass via the formation of short-lived cages, which act both on the vibrational and the diffusive parts of the single-particle motion. After operating a standard data reduction and the subtraction of the Ne signal, experimental neutron spectra were analyzed through a generalization of the Young and Koppel model, and the H_2 center-of-mass self-dynamic structure factor was finally extracted for the two liquid samples. Important physical quantities (namely, single-particle mean kinetic energy and self-diffusion coefficient) were estimated from the experimental data and then compared with quantum dynamical calculations, which also provided simulations of the velocity autocorrelation functions for Ne atoms and H_2 centers of mass. The latter estimates, in the framework of the well-known Gaussian approximation, were used to simulate the H_2 center-of-mass self-dynamic structure factor in the same kinematic range and thermodynamic conditions of the neutron scattering one. The comparison between measured and calculated spectra turned out to be qualitatively good, but some discrepancies, especially in the low-frequency part, seem to reinforce the idea of the existence of relevant non-Gaussian effects as in the case of pure hydrogen and H_2-D_2 mixtures.

I. INTRODUCTION

Understanding the microscopic dynamics of semiquantum liquids, i.e., liquid systems exhibiting moderate quantum effects, such as H_2, D_2, and Ne, is still considered to be an interesting (and partially unsolved) problem in condensed matter physics [1]. In general, semiquantum liquids do not freeze at temperatures lower than their Debye temperature [2]. However, differently from the extreme quantum fluids (e.g., superfluid He isotopes, ultracold atoms, etc.), quantum statistics plays no important role in the translational dynamics of the particles composing these systems [2], so that it is possible to make use of the Maxwell-Boltzmann statistics to describe most of the properties of semiquantum liquids. Given this situation, any precise experimental determination of dynamic quantities (i.e., time-correlation functions or their frequency spectra) related to these liquids that can be compared to corresponding theoretical predictions becomes quite valuable, like, for instance, recent neutron scattering experiments on hydrogen [3] and its isotopic mixtures [4]. In these two studies, the authors have obtained experimental estimates of the self-dynamic structure factor [5] of H_2 *centers of mass* (CMs) in pure bulk liquid and mixed with liquid deuterium, both at low temperature. These systems were selected because the interaction between thermal neutrons and H_2 makes it possible to

single out the self-dynamics (i.e., incoherent) of the molecular CMs [5]. This is because the coherent cross section of neutron scattering from H_2 is much smaller than the incoherent one so contributions to the inelastic neutron scattering signal from correlated motions are negligible. Now, it is common practice to connect the mentioned self-dynamic structure factor (also known as self-scattering law) to the power spectrum of the velocity autocorrelation function (VACF). This connection is generally attempted by means of the so-called Gaussian approximation (GA) [6], which owes its name to the assumption that the self-intermediate scattering function [5] is given by

$$I_s(Q, t) = \exp\left[-\tfrac{1}{3} Q^2 w(t)\right], \qquad (1)$$

where $w(t)$ is the time-dependent mean squared displacement of the scattering nucleus. In this respect, the cited works on H_2 and H_2-D_2 [3,4] provided clear experimental evidences of a GA failure rather larger than in liquid argon [7], possibly due to the more quantum delocalized nature of the hydrogen molecule. Thus, the purpose of this study is to investigate the GA when applied to hydrogen impurities in Ne. A low-concentration H_2 solution in liquid Ne shows an equation of state quite different from the pure hydrogen one and much closer to that of pure neon. In particular, it is possible to achieve high molecular densities remaining in the liquid state. In addition, the system is interesting from the microscopic point of view: the H_2-H_2 and Ne-Ne pair potentials are very similar to each other, so it is not incorrect to think of a hydrogen molecule as a sort of "light" neon atom, at least from

---

*Corresponding author: d.colognesi@ifac.cnr.it

the center-of-mass point of view. In this way, our solution may be seen as a collection of similar particles, a small fraction of which is more quantum delocalized than the rest. Here, the quantum character of H_2 is even stronger than in the two previous cases (i.e., H_2 and H_2-D_2), as shown by a higher zero-point CM mean kinetic energy [8,9]. As a matter of fact, a typical quantum feature of these systems is represented by the value of single-particle mean kinetic energy: due to the zero-point particle motion, one observes that the ground-state component of the kinetic energy is not negligible if compared to the thermal component of the same quantity [10]. In addition, one can hypothesize a higher value of the activation energy [11] of the hydrogen self-diffusion coefficient since the diffusional motion of H_2 could be hindered by an increased particle density and, moreover, by the possible formation of Ne pseudocages around the hydrogen molecule. These short-lived structures might be more effective in the Ne case than in the D_2 one due to the much larger particle mass. Last but not least, it is worth noting that there already exist preliminary neutron spectra [9,12] on some neon-hydrogen liquid mixtures, recorded at high resolution but at constant scattering angle (i.e., with a variable momentum transfer) on the TOSCA-II spectrometer. They actually exhibit large deviations from the GA (see Fig. 2 in Ref. [12]), at least at a semiqualitative level, in a narrow momentum transfer interval.

The rest of this paper will be organized as follows: The experimental procedure will be described in detail in Sec. II, while in Sec. III we will determine the self-dynamic structure factor of H_2 CMs, starting from the experimental neutron spectra. Section IV will be fully devoted to the computational details concerning the quantum dynamics simulations performed on the Ne-H_2 mixtures under investigation, in order to extract their VACFs. In Sec. V, we will discuss the obtained results and will check the validity of the GA: the physical quantities derived from the experimental spectra will be compared to their estimates obtained from the aforementioned quantum simulations. Finally, Sec. VI will be devoted to conclusions and perspectives.

II. EXPERIMENTAL DETAILS

Inelastic neutron scattering measurements were performed on MARI [13], a spectrometer installed at the ISIS Neutron and Muon Source (Rutherford Appleton Laboratory, United Kingdom). MARI is a direct-geometry spectrometer based on the time-of-flight technique: the incoming neutron energy E_0 is selected by a Fermi chopper prior to the scattering event, while the final neutron energy E_1 is determined from the time of arrival of the neutrons which are first scattered and then detected. The angular range available on the instrument ($3.43° < \theta < 134.13°$) is almost continuously covered by ^{3}He-gas detectors in steps of $0.43°$. Using an appropriate value of the incident energy $E_0 = 62.0$ meV, we have been able to explore a wide zone of the (Q, ω) kinematic plane, namely, $2.0 \text{ Å}^{-1} \leqslant Q \leqslant 8.5 \text{ Å}^{-1}$, $\hbar\omega \lesssim 60.0$ meV, with $\hbar\omega$ being the energy transfer and $\hbar Q$ the momentum transfer modulus. The MARI energy transfer resolution ($\Delta\hbar\omega$) is determined by the frequency and the type of Fermi chopper employed in the measurements. In our case, a medium resolution option (i.e., a Gd-slits chopper spinning at 400 Hz) was

TABLE I. Thermodynamic conditions of the measured liquid samples, including sample number, species, temperature T, hydrogen concentration $c[H_2]$, pressure p, total molecular density n, and integrated proton current IC. Estimated uncertainties are reported in parentheses.

No.	Species	T (K)	$c[H_2]$ (%)	p (bar)	n (nm^{-3})	IC (μA h)
1	Vanadium	293(1)				904.2
2	Empty can	30.08(3)				3478.0
3	Pure Ne	30.2(3)		2.27(4)	34.3(2)	2147.8
4	Ne-H_2	30.1(1)	10(1)	7.1(3)	31.0(4)	4157.5
5	Ne-H_2	30.08(3)	3.4(3)	4.7(2)	33.1(2)	5464.0

selected, resulting in values of $\Delta\hbar\omega$ at zero energy transfer (i.e., at the so-called *elastic line*) ranging from 2.02 meV at the lowest scattering angles to 3.20 meV at the highest one, experimentally determined via standard vanadium measurements. Since the measured data concerning the elastic line zone and actually used in the rest of this study come from detectors placed at $\theta \leqslant 60.4°$, we have always employed an averaged value of the resolution at $\omega = 0$, namely, $\Delta\hbar\omega(\omega = 0) = 2.37$ meV, unless explicitly stated in the text. As for the $\Delta\hbar\omega$ values at $\omega > 0$, estimates obtained from routines available on the spectrometer were considered.

A comprehensive description of the samples (including species, temperature, hydrogen concentration, pressure, total molecular density, and integrated proton current) can be found in Table I. Temperature and pressure were monitored during the measurements, and the total molecular density calculated from these and various thermodynamic data available in the literature: Ref. [14] for pure neon, Ref. [15] for pure hydrogen, and Refs. [16,17] for neon-hydrogen mixtures. Another important issue was the rotational population (labeled by the quantum number j) of the hydrogen molecules composing the experimental samples, namely, either ortho-hydrogen (o-H_2, odd j) or para-hydrogen (p-H_2, even j) species. As it will be made clear later, *normal hydrogen* (n-H_2) has been always employed in this experiment. This is hydrogen in which the ortho-para distribution is not in thermodynamic equilibrium at the actual (low) temperature of the sample (like, on the contrary, for the so-called equilibrium hydrogen e-H_2), but is still in equilibrium at room temperature: $c[o$-$H_2]/c[n$-$H_2] = 75\%$ [15]. This is possible since spontaneous low-temperature ortho-para conversion proceeds very slowly (typical time of the order of several days [18]) in the liquid phase, if an appropriate catalyst is not present. The choice to employ n-H_2 instead of pure p-H_2 was dictated by experimental reasons linked with the long preparation time of the Ne-H_2 mixture at room temperature in the gas phase. As a matter of fact, p-H_2 would have been potentially unstable (back conversion from p-H_2 to o-H_2) giving rise to a condensed mixture with an unknown ortho-para ratio. The method used to experimentally check this ratio during the experiment will be explained later.

After performing the calibration measurement at room temperature making use of an appropriate vanadium annulus, we inserted the sample container (i.e., the scattering cell) into the instrumental sample chamber equipped with a closed cycle

refrigerator, we cooled it down to the desired temperature (i.e., $T = 30$ K), and then we measured the empty cell neutron spectrum for a counting time of about 19.5 h. The cell was made of an aluminum alloy with a circular-slab geometry (annulus) and consisted of two concentric cylinders giving rise to a 2.0-mm void to be filled with the liquid mixture sample exhibiting an average diameter of 42.0 mm. Unlike other neutron spectrometers, the MARI detectors lie below the sample in a vertical scattering plane. Thus, the annulus axis was perpendicular to the neutron beam, but horizontal rather than vertical as usual. The external diameter of the container was almost coinciding with the vertical beam size (about 50 mm, including penumbra), while the container total length (70.0 mm) was rather bigger than the horizontal beam size (still about 50 mm, including penumbra), so the cell was masked with boron nitride ceramics in order to exclude its bulky ends which contained screws, seals, and no liquid sample. In this way, the portion of cell irradiated by neutrons was reduced to approximately 45 mm in length.

Subsequently, the temperature of the cell was increased to $T = 33$ K and neon gas (*CK Special Gases*, 99.997% assay) was allowed to condense in it. The pressure of the gas handling system was initially set to about $p = 4.5$ bar (somewhat larger than the corresponding saturated vapor pressure SVP = 2.2381 bar [14]). Then, the cell temperature was slowly (in order to prevent the formation of solid plugs in the tubes) decreased to $T = 15$ K where the pressure reached the final value of $p = 0.354$ bar with Ne frozen in the sample container. At this stage, knowing the exact initial volume of the neon gas in the handling system, we were sure that the cell was completely filled with the sample. Later, the temperature was raised again to 30 K, the pressure was adjusted to $p = 2.3$ bar, and a neutron measurement of sample No. 3 was started (see Table I), lasting for about 15 h. The stability of the thermodynamic conditions during this measurement was not perfect although still fully acceptable: temperature and pressure uncertainties were estimated to be around 0.3 K and 0.04 bar, respectively.

As for the mixed samples No. 4 and No. 5 (see again Table I), they were obtained in a different and more elaborate way. Let us summarize the main steps of the procedure followed to produce the No. 4, $c[H_2] = 10\%$, liquid mixture, recalling that the No. 5, $c[H_2] = 3.4\%$, one was prepared similarly. An appropriate amount of normal hydrogen gas (*CK Special Gases*, 99.99% assay) was mixed with the aforementioned neon gas in a buffer volume at room temperature under a total pressure of about 4.13 bar. The exact amount of gaseous mixture needed to fill up the sample cell (identical to the can already used for pure Ne) with liquid was condensed in it at $T = 28$ K. Then, the cell was slowly cooled down to $T = 4$ K, so to decrease the vapor pressure of the gas handling line to an extremely low value of few mbar. This step was regarded as very important in order to prevent an undesired separation of the mixture, where the more volatile gas (i.e., H_2) could concentrate in the buffer volume, while the less volatile (i.e., Ne) condensed in the coldest point of the gas line, namely, in the sample cell. This would have altered the mixture composition in quite a noticeable way. At the end, the sample can was isolated from the rest of the gas handling line and warmed up to the requested experimental temperature

(i.e., 30 K) where an internal pressure, oscillating in the range 6.5–7.5 bar, built up spontaneously. This instability was considered as fully natural since the sample had necessarily to cross a narrow two-liquid zone [19] before reaching, at $T = 29.00$ K, the single-liquid zone, safely stable for all hydrogen concentrations [17]. Thus, after a long equilibration time of the order of 2 h (carefully monitored through the sample pressure), the neutron measurement of sample No. 4 started, lasting for about 35 h, divided in two equal subruns. Finally, sample No. 5 was prepared, condensed, stabilized, and measured for 40.75 h, still divided in two equal subruns.

III. DATA ANALYSIS

At the end of the neutron scattering experiment on MARI, raw time-of-flight data were normalized to the incoming neutron counts of the monitor, purged of contributions from noisy tubes, and corrected for detector efficiency. Subsequently, processed time-of-flight data were transformed into energy transfer spectra, removing the well-known kinematic factor $(E_1/E_0)^{1/2}$ [5] and performing the appropriate rebinning. Finally, the usual vanadium spectra normalization was performed, taking into account the minute angular effect due to the Debye-Waller factor of this metal. The outputs of this part of the data analysis procedure were the so-called $\Sigma(\theta, \omega)$ spectra, particularly suitable for the following operations: (i) empty can scattering subtraction after considering sample attenuation; (ii) sample self-shielding evaluation and correction. Both points (i) and (ii) were implemented using numerical integration routines which approximately calculated the scattering attenuation from the sample cell in the two conditions: empty and filled with the three mentioned samples, namely, Nos. 3–5. In the last two of these calculations, concerning the total cross section of the respective Ne-H_2 mixture, a proper linear combination of the total scattering cross section of neon [20], $\sigma_{t, \text{Ne}}$, with that of liquid normal hydrogen at $T = 16$ K [21], $\sigma_{t, \text{n-}H_2}(E_0)$, was assumed to be accurate enough for the self-shielding correction. As for the possible multiple scattering contaminations, considering the high values of the liquid sample transmission at $E_0 = 62$ meV (namely, 94.7%, 86.5%, and 91.6%, respectively, for Nos. 3, 4, and 5), no correction was performed.

At this stage, $\Sigma(\theta, \omega)$ spectra were transformed into constant-Q data, $\Sigma(Q, \omega)$, through standard binning routines. This transformation made possible the determination of inelastic spectra at Q values approximately ranging in the interval 2.0 Å^{-1} < Q < 8.5 Å^{-1} in steps of 0.5 Å^{-1}. The following phase of the data reduction procedure included the subtraction of the scattering due to neon from the spectra of samples No. 4 and No. 5. This was accomplished making use of the experimental pure neon spectrum (i.e., sample No. 3), properly scaled to account for sample molecular densities and Ne concentrations, as carefully explained in Appendix A. After this subtraction, processed neutron spectroscopic data essentially contained only scattering from n-H_2 and so could be dubbed as $\Sigma_{n\text{-}H_2}(Q, \omega)$ and, in the present energy transfer range, included only six relevant rotational terms, which were related to the $j = 0, 1 \rightarrow j' = 0, 1, 2$ hydrogen transitions. Neglecting the small coherent scattering contribution due to the so-called *distinct* term (as shown in Appendix A), one
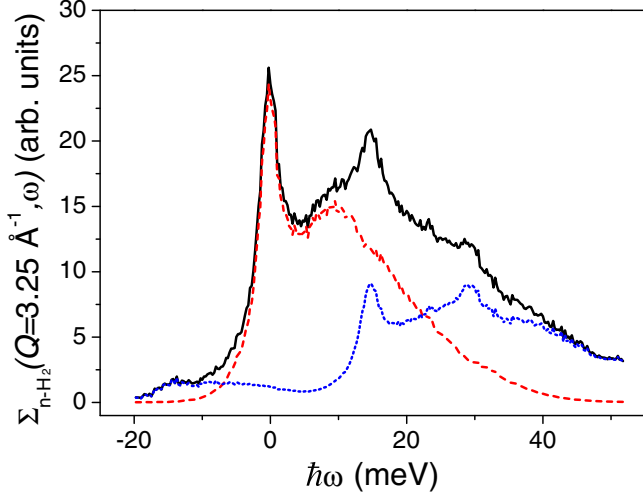
FIG. 1. Example of subtraction of the unwanted rotational contributions from the experimental n-H_2 spectrum derived from a neon-hydrogen liquid mixture (sample No. (4), $c[H_2] = 10\%$, $T = 30.1$ K). All plotted data have been measured at $Q = 3.25$ Å^{-1}. The full black line represents the original spectrum (including various rotational contributions together with the $j = 1 \rightarrow j' = 1$ one), dotted blue line stands for all the unwanted rotational contributions, while the dashed red one is their difference amounting to the $j = 1 \rightarrow j' = 1$ contribution only.

could relate the experimental $\Sigma_{n\text{-}H_2}(Q, \omega)$ to the self-part of the H_2 CM dynamic structure factor $S_{s,CM}(Q, \omega)$ making use of the so-called "generalized Young and Koppel model" [22–24]:

$$\Sigma_{n\text{-}H_2}(Q, \omega) = \sum_{j=0}^{1} x_j \sum_{j'=0}^{2} \left(\frac{\sigma_{j,j'}}{4\pi} \right) f_{j,j'}(Q) \, S_{s,CM}(Q, \omega)$$
$$\otimes \, \delta(\hbar\omega - E_{j,j'}), \quad (2)$$

where x_j is the relative population of the rotational species j, $\sigma_{j,j'}$ is the neutron scattering cross section for the $j \rightarrow j'$ rotational transition, while $f_{j,j'}(Q)$ and $E_{j,j'}$ are the molecular form factor and the energy shift for this transition, respectively. This model, which does not include semiclassical approximations, is based on the assumption that the free rotational dynamics of H_2 may be separated from the many-body CM one. Although this assumption might generally sound rather peculiar as far as neutron scattering from H_2 and D_2 is concerned, it has been successfully applied in a large number of condensed matter systems (see Refs. [25,26] for two early examples). As a matter of fact, our neutron experimental spectra could be understood as a "comb" of replicas of $S_{s,CM}(Q, \omega)$, shifted by $E_{j,j'}$ and weighted by the population and cross-section terms $x_j \, \sigma_{j,j'}$, as well as by the Q-dependent form factor $f_{j,j'}(Q)$. While transitions $j = 0 \rightarrow j' = 0, 2$ are intrinsically rather weak [22–24] for all the momentum transfer values experimentally available, the other four transitions, i.e., $j = 0 \rightarrow j' = 1$ and $j = 1 \rightarrow j' = 0, 1, 2$, were actually directly visible in the $\Sigma_{n\text{-}H_2}(Q, \omega)$ spectra (as shown in the example reported in Fig. 1) with $j = 1 \rightarrow j' = 1$ being clearly the strongest up to about 4 Å^{-1} in both mixtures. In this way, it was possible to single out

the $j = 1 \rightarrow j' = 1$ term through a two-step procedure: first, a simple multi-Gaussian fit to work out the ratio $R_Q(\omega)$ between the unwanted rotational contributions and the original spectrum (including all the mentioned rotational terms); second, the product between $\Sigma_{n\text{-}H_2}(Q, \omega)$ and $[1 - R_Q(\omega)]$ to obtain the difference spectrum amounting to the $j = 1 \rightarrow j' = 1$ contribution only. This procedure (an example of which can be found in Fig. 1) was accomplished starting from the data set with 2.0 Å$^{-1} < Q < 2.5$ Å^{-1} (i.e., average $Q = 2.25$ Å^{-1}) up to that with 5.0 Å$^{-1} < Q < 5.5$ Å^{-1} (i.e., average $Q = 5.25$ Å^{-1}) for both mixtures. Final CM spectra have been reported in Figs. 2 and 3 for samples No. 4 and 5, respectively.
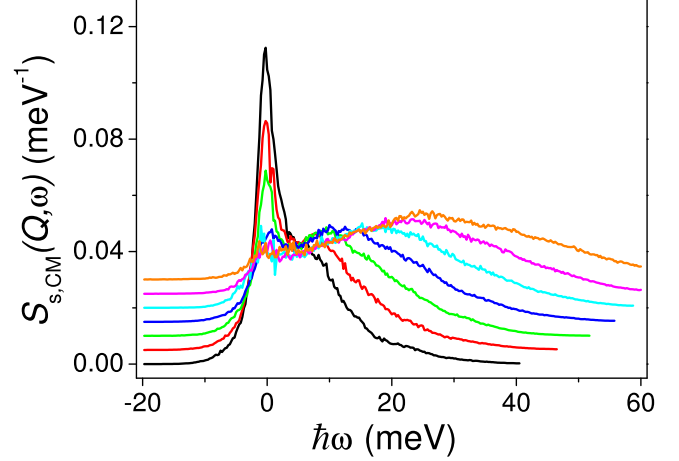

FIG. 2. Experimental self-scattering law for H_2 centers of mass in the neon-hydrogen liquid mixture of sample No. 4 ($c[H_2] = 10\%$, $T = 30.1$ K). Reported spectra range from $Q = 2.25$ Å^{-1} (lowest black line) to $Q = 5.25$ Å^{-1} (upmost orange line) with a 0.5-Å^{-1} step. Curves have been vertically shifted for graphic reasons.
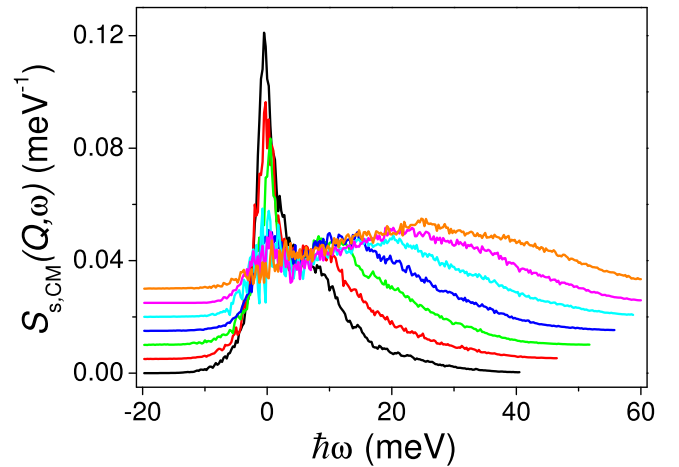

FIG. 3. Experimental self-scattering law for H_2 centers of mass in the neon-hydrogen liquid mixture of sample No. 5 ($c[H_2] = 3.4\%$, $T = 30.08$ K). Reported spectra range from $Q = 2.25$ Å^{-1} (lowest black line) to $Q = 5.25$ Å^{-1} (upmost orange line) with a 0.5-Å^{-1} step. Curves have been vertically shifted for graphic reasons.

Before concluding this section, it is worthwhile to spend a few words on a by-product of the Eq. (2) implementation. From the mentioned fitting procedure it was possible to estimate the experimental values of $x_{j=0,1}$ (i.e., $c[p\text{-}H_2]/c[H_2]$ and $c[o\text{-}H_2]/c[H_2]$ in our case), not only for the two summed runs on the mixture samples, but also for the four partial subruns cited in Sec. II. So, we could verify that the H_2 rotational population contained in the two mixtures was essentially stable during the measurement, with just a small trend towards a low-temperature ortho-para conversion for the latter subrun compared with the former.

IV. QUANTUM DYNAMICS SIMULATIONS

In order to provide the H_2-CM VACFs required for the analysis of the experimental spectra from samples No. 4 and No. 5, we performed a series of centroid molecular dynamics (CMD) simulations [27]. In these simulations, the interactions have been taken to be strictly pairwise additive according to the following scheme:

(a) those between two Ne atoms were modeled by a spherically symmetric Aziz HFD-B potential [28];

(b) those between an H_2 CM and a neon atom were modeled by the orientation-dependent semiempirical potential developed by Faubel *et al.* [29]; however, in order to deal with the H_2 CM rather than a molecular dumbbell, a spherical average was performed following the procedure devised by Challa and Johnson [30] for a path integral Monte Carlo (PIMC) calculation on hydrogen-neon mixtures;

(c) those between two H_2 CMs were modeled by the spherically symmetric Silvera-Goldman potential [31].

Further details about the Ne-Ne pair potential have been reported in Appendix B.

In our calculations, the total number of molecules was kept at $N = N[Ne] + N[H_2] = 256$. Since most of the simulations were performed before the experiments, when the exact experimental conditions were still unknown, we initially decided to investigate a series of thermodynamic states in the range of 4%–20% H_2 concentration, in steps of 4%, corresponding to H_2 particle numbers 10, 20, 31, 41, and 51, plus simulations of pure Ne and H_2 as reference systems. These were later complemented by runs with $N[H_2] = 6, 9, 22, 26$, and 27, in order to better approximate the actual experimental conditions of Nos. 4 and 5 in Table I. Finally, two smaller-volume simulations ($N = 108$) with $N[H_2] = 4$ and 11 were also performed to check possible finite size effects. Their importance has been found to be rather modest. All our simulations were performed at a uniform temperature of $T = 30$ K and at the total molecular densities listed in Table II, which were obtained by interpolating the concentration-density data of Güsewell *et al.* [16] by a polynomial fit.

Since CMD is basically a classical molecular dynamics technique in a quantum mechanical force field, we have calculated these forces by very short PIMC simulations at each time step, using the so-called *primitive algorithm* [32] and a Trotter number of $P = 64$ for the number of beads on the classical ring polymers replacing the quantum particles in PIMC. Although more time consuming than the usual implementation, this avoids sampling problems due to the stiff internal modes of the polymers and allowed us to use a time
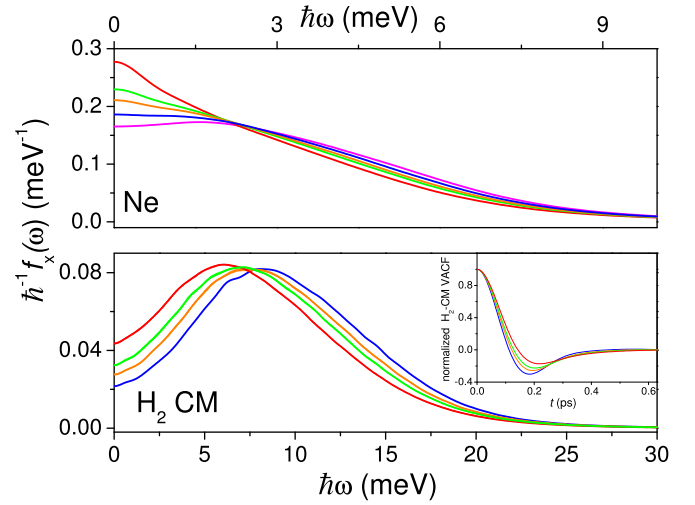

FIG. 4. Simulated spectral functions $f_x(\omega)$ for $x = $ CM (hydrogen centers of mass, lower panel) and for $x = $ Ne (neon atoms, upper panel) in some selected neon-hydrogen mixtures reported in Table II, from bottom to top at low frequency, according to the following color code: (i) magenta, (iv) blue, (vi) orange, (ix) green, and (xi) red. In the inset, following the same color code, the canonical velocity autocorrelation functions for the H_2 center of mass have been plotted after performing a standard normalization procedure (i.e. equal to 1 at $t = 0$).

step $\Delta t = 0.005$ ps. The classical dynamics was kept at a temperature $T = 30$ K by means of a Gaussian thermostat [33], and the total molecular densities of the mixtures were taken from Ref. [16], as explained above. At each thermodynamic state we have performed 10 independent runs of 10^5 time steps (500 ps) each, in order to get an estimate of the statistical uncertainty of the results. The VACFs were calculated up to a maximum time lag of 5 ps and multiplied by a Welch window [34] before Fourier transforming. The evolution of the VACF for the H_2 CM as a function of the hydrogen concentration is plotted in the inset of Fig. 4 for some selected thermodynamic conditions among those listed in Table II: as the mixture molecular density decreases because of the H_2 concentration growth, the negative dip of the normalized (i.e., equal to one at $t = 0$) VACF becomes shallower and shallower.

Since a CMD simulation yields the *canonical* or Kubo transformed [35] $\langle \vec{v}(0) \cdot \vec{v}(t) \rangle_x^{(k)}$ (with $x = $ "Ne" or "CM"), rather than the proper quantum mechanical VACF for Ne atoms and H_2 CMs, the spectral functions $f_x(\omega)$ were obtained from the relationship

$$f_x(\omega) = \frac{m_x}{3\pi k_B T} \int_{-\infty}^{\infty} \exp(-i\omega t)\langle \vec{v}(0) \cdot \vec{v}(t) \rangle_x^{(k)} dt, \quad (3)$$

where m_x represents the particle mass (i.e., either the neon or the H_2 mass). So, except for the $m_x/(3\pi k_B T)$ factor, which guarantees an appropriate normalization, $f_x(\omega)$ is simply given by the Fourier transform of the canonical VACF. These physical quantities, both for Ne and H_2 CM, are plotted in Fig. 4 for some selected thermodynamic conditions among those listed in Table II. The distinct vibrational behavior of Ne with respect to the H_2 CM one is clearly visible in this figure and is very roughly accountable via a simple

TABLE II. Thermodynamic conditions of the liquid samples simulated at $T = 30.0$ K and computational results, including simulation number, total number of particles N, number of H_2 molecules $N[H_2]$, hydrogen concentration $c[H_2]$, total molecular density n, self-diffusion coefficient D_s for H_2 CM and Ne, mean kinetic energy $\langle E_k \rangle^{(sp)}$ from VACF spectra for H_2 CM and Ne, mean kinetic energy $\langle E_k \rangle^{(po)}$ from PIMC "polymers" for H_2 CM and Ne. See main text for details.

No.	N	$N[H_2]$	$c[H_2]$ (%)	n (nm^{-3})	$D_{s,\mathrm{CM}}$ (10^{-5} cm^2 s^{-1})	$D_{s,\mathrm{Ne}}$ (10^{-5} cm^2 s^{-1})	$\langle E_k \rangle^{(sp)}_{\mathrm{CM}}$ (K)	$\langle E_k \rangle^{(sp)}_{\mathrm{Ne}}$ (K)	$\langle E_k \rangle^{(po)}_{\mathrm{CM}}$ (K)	$\langle E_k \rangle^{(po)}_{\mathrm{Ne}}$ (K)
i	256	0	0.00	34.44		2.111(4)		54.31(1)		54.18(1)
ii	256	6	2.34	33.48	2.58(2)	2.284(8)	93.8(2)	53.95(1)	94.3(1)	53.83(1)
iii	256	9	3.52	33.07	2.71(4)	2.36(1)	92.6(2)	53.82(1)	93.1(2)	53.69(1)
iv	256	10	3.91	32.94	2.76(2)	2.377(8)	92.3(1)	53.78(1)	92.8(1)	53.65(1)
v	256	20	7.81	31.66	3.42(2)	2.653(6)	88.8(1)	53.36(1)	89.2(1)	53.25(1)
vi	256	22	8.59	31.42	3.53(3)	2.69(1)	88.4(1)	53.29(1)	88.79(8)	53.18(1)
vii	256	26	10.16	30.94	3.78(4)	2.82(1)	87.4(1)	53.15(1)	87.8(1)	53.03(1)
viii	256	27	10.55	30.82	3.86(5)	2.845(8)	87.1(2)	53.09(1)	87.5(2)	52.98(1)
ix	256	31	12.11	30.36	4.15(4)	2.93(1)	85.7(2)	52.97(1)	86.2(2)	52.86(1)
x	256	41	16.02	29.23	4.93(6)	3.24(1)	83.5(1)	52.64(1)	83.9(1)	52.53(1)
xi	256	51	19.92	28.15	5.57(4)	3.54(1)	81.65(7)	52.29(1)	81.98(6)	52.20(1)
xii	256	256	100.00	16.08	25.73(4)		63.34(1)		63.50(1)	
xiii	108	4	3.70	33.01	2.59(1)	2.29(1)	93.48(6)	53.80(1)	93.98(7)	53.62(1)
xiv	108	11	10.19	30.93	3.50(1)	2.73(1)	88.34(4)	53.08(1)	88.71(3)	52.94(1)

mass-ratio scaling applied to the abscissa axis: $\omega_{\mathrm{CM}}/\omega_{\mathrm{Ne}} \approx (m_{\mathrm{Ne}}/m_{\mathrm{CM}})^{0.5} = 3.164$ since the respective (i.e., Ne-Ne and CM-Ne) interparticle potentials are quite similar (see below for details). However, after taking a closer look, one can see that the low frequency parts of the hydrogen and neon data sets are indeed quite different: H_2 CM spectra appear almost solidlike with $f_{\mathrm{CM}}(\omega)$ growing from low values at $\omega \approx 0$ to a clear maximum (possibly the "cage rattling" frequency), and then slowly decreasing to zero with a long tail. On the contrary, Ne exhibits the typical diluted-fluid behavior, which is almost monotonic, as the maximum of $f_{\mathrm{Ne}}(\omega)$ (at $\omega > 0$) is very weak or even completely missing. In addition, the decrease of the system total molecular density n, induced by the increase of the hydrogen concentration, acts on the two types of $f_x(\omega)$ in a dissimilar way: in H_2 CM this effect is clearly visible both in the change of $f_{\mathrm{CM}}(0)$ and in a general frequency variation via a large kinetic-energy Grüneisen parameter $\gamma = (n/\langle E_k \rangle)(\partial \langle E_k \rangle/\partial n)$ [$\gamma_{\mathrm{CM}} = 1.16(6)$], while in Ne this frequency variation is more modest [$\gamma_{\mathrm{Ne}} = 0.88(1)$] and the main change is restricted to the area around $\omega \approx 0$, which has a clear diffusional character [6]. Surely, the feature we have just mentioned [i.e., the marked peak in the spectral function $f_{\mathrm{CM}}(\omega)$ interpreted as an effect of "caging"] is not specific to the quantum nature of diluted solutions of H_2 in liquid Ne. On the contrary, it is generally exhibited by all dense fluids (either classical or quantum) when their molecular density approaches the value pertaining to the liquid at the triple point n_{tp}. For instance, a detailed description of this phenomenon has been recently shown in Fig. 11 of Ref. [36], dealing with supercritical classical Lennard-Jones fluids. However, our present systems have their own specific behavior: first, the molecular density of the two samples (see Table I) is not very close to the n_{tp} of pure neon (namely, 37.21 nm^{-3} [14]). Even getting rid of the system "swelling" due to hydrogen (i.e., reducing the H_2 amount to zero), the liquid Ne molecular density (at $T \approx 30$ K and relatively low pressure) grows only to about 34.3 nm^{-3}. Under these conditions, it is not surprising that the Ne self-dynamics is far from

that of a dense liquid as shown in the upper panel of Fig. 4, where the $f_{\mathrm{Ne}}(\omega)$ spectra of the Ne velocity autocorrelation function do not exhibit the strong peak mentioned above. Just the magenta line (i.e., that at $c[H_2] = 0\%$) shows a very weak trend in this direction. Second, the physical picture we have just described, which applies to Ne atoms, is not valid for H_2 centers of mass. This fact can be rationalized considering that the normal hydrogen n_{tp} (which amounts to 23.06 nm^{-3} [15]) is much smaller than the molecular density of our samples. This means that our solution samples are an artificial environment for H_2 corresponding to "superdense" liquids which do not exist in the pure H_2 phase (at $T = 30$ K) since the maximum molecular density of liquid normal hydrogen is only about 29.31 nm^{-3} (on the freezing line at $p = 733.5$ bar [15]).

An important piece of information contained in these spectra is the self-diffusion coefficient D_s of the molecules, which is determined, as we have just mentioned, by the zero frequency value of $f_x(\omega)$. For example, in the case of hydrogen one reads as

$$D_{s,\mathrm{CM}} = \frac{\pi k_B T}{2 m_{\mathrm{CM}}} f_{\mathrm{CM}}(0) = \frac{1}{3} \int_0^\infty \langle \vec{v}(0) \cdot \vec{v}(t) \rangle^{(k)}_{\mathrm{CM}} dt. \quad (4)$$

Our CMD predictions for the self-diffusion coefficients for H_2 CM, as well as for Ne, are included in Table II and in Fig. 5. Note that the uncertainties given there are merely the statistical errors and that the actual values may be slightly different since the self-diffusion coefficient is known to weakly depend on the system size [37].

Another important and easily accessible physical quantity is the mean kinetic energy of a neon atom and a hydrogen molecule CM, $\langle E_k \rangle_x$ (with $x = $ "Ne" or "CM"). Interestingly, there are two routes to this property in CMD simulations. As in PIMC simulations, the mean kinetic energy may be calculated from the average potential energy stored in the "springs" of the polymers. Although this "crude energy estimator" [38] of $\langle E_k \rangle_x$ is considered to be inferior to, e.g., the virial estimator [39], the statistical uncertainties were quite
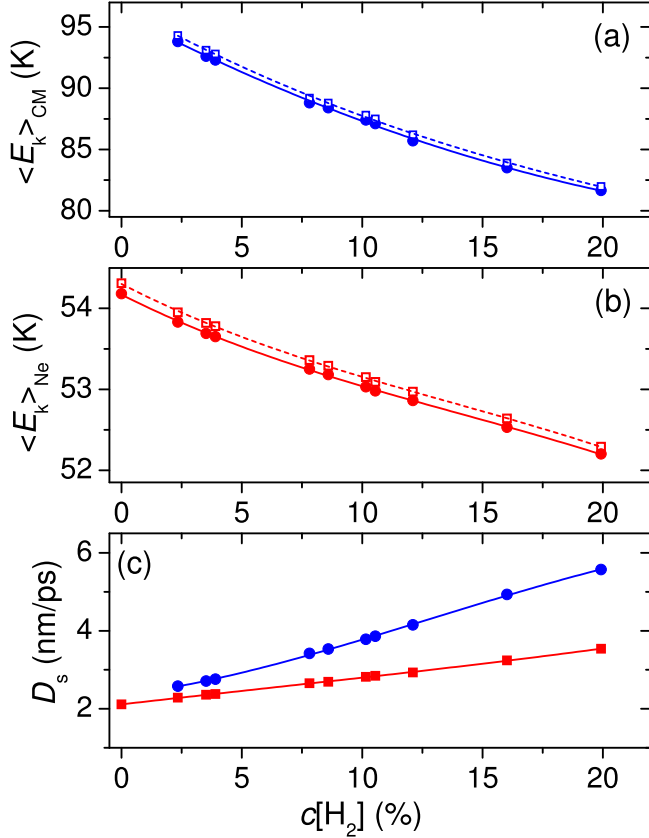
FIG. 6. Simulated self-scattering law for H_2 centers of mass in a neon-hydrogen liquid mixture (sample No. 4, $c[H_2] = 10\%$, $T = 30.1$ K) from centroid molecular dynamics data via the Gaussian approximation. Reported spectra range from $Q = 2.25$ Å^{-1} (lowest black line) to $Q = 5.25$ Å^{-1} (upmost orange line) with a 0.5-Å^{-1} step. Experimental data from Fig. 2 have been also plotted for comparison. Curves have been vertically shifted for graphic reasons. In the inset, same simulated data have been reported in a wider energy transfer range (no shift applied).

FIG. 5. Data derived from the CMD simulations of liquid samples ($T = 30.0$ K) reported in Table II. (a) Shows the mean kinetic energy of the H_2 centers of mass evaluated according to the two different procedures described in the main text: VACF spectra (full blue circles) and PIMC "polymers" (empty blue squares). (b) Exhibits the same quantities as in (a), but for Ne atoms: VACF spectra (full red circles) and PIMC "polymers" (empty red squares). (c) Reports the self-diffusion coefficients of both H_2 centers of mass (full blue circles) and Ne atoms (full red squares). Full and dashed lines in the three panels are simple polynomial fits and represent only guides for the eyes.

small in our case and probably smaller than the systematic error due to the finite Trotter number P. Alternatively, the mean kinetic energy may also be calculated from the spectral function $f_x(\omega)$ [40]. In the case of the hydrogen CM, one reads as

$$\langle E_k \rangle_{CM} = \frac{3}{4} \hbar \int_0^\infty \omega \coth \left(\frac{\hbar \omega}{2 k_B T} \right) f_{CM}(\omega) d\omega. \quad (5)$$

Obviously, this prediction is likewise affected by the finite value of P, but also by the overall quality of the simulated VACF and the specific way (such as windowing) in which $f_{CM}(\omega)$ is calculated via Eq. (3). Both estimates of the mean kinetic energy of H_2 centers of mass and Ne atoms are reported in Table II and in Fig. 5 and should be contrasted to the value of 45 K for a classical system at $T = 30$ K. It is also worth noting that the H_2-CM mean kinetic energy rises to values well above 90 K as the concentration decreases, which is much larger than in pure hydrogen, where we have calculated a value of about 63.4 K.
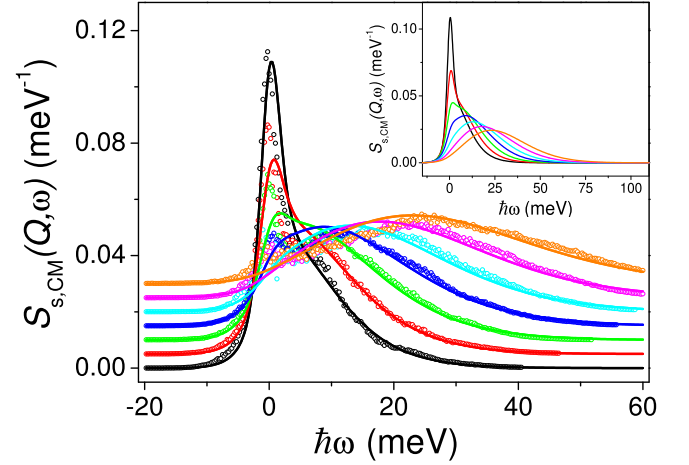
Finally, the GA expression [6] for the self-intermediate scattering function was applied to $f_{CM}(\omega)$:

$$I_{s,CM}^{(GA)}(Q,t) = \exp \left\{ -\frac{\hbar Q^2}{2 m_{CM}} \int_0^\infty \frac{f_{CM}(\omega)}{\omega} \left[\coth \left(\frac{\hbar \omega}{2 k_B T} \right) \right. \right.$$
$$\left. \left. \times [1 - \cos(\omega t)] - i \, \sin(\omega t) \right] d\omega \right\}, \quad (6)$$

in order to yield simulated neutron scattering spectra. These, including the instrumental energy resolution discussed in Sec. II as well as the average over the appropriate Q slice, were dubbed $S_{s,CM}^{(GA)}(Q, \omega)$ and are reported in Figs. 6 and 7 for samples No. 4 and No. 5, respectively, for the usual Q values from 2.25 to 5.25 Å^{-1}.

V. DISCUSSION

In order to start studying the obtained experimental CM spectra $S_{s,CM}(Q, \omega)$, we have performed a normalization to unity, which is appropriate for self-dynamics [5]. In doing so, a high energy extrapolation has been accomplished in order to include the small spectral zones placed out of the available energy transfer ranges. For the last three Q values, namely, 4.25, 4.75, and 5.25 Å^{-1}, this treatment was slightly more relevant and might have induced some level of uncertainty, even though the following careful procedure has been applied: we have started from the simulated spectra $S_{s,CM}^{(GA)}(Q, \omega)$ (broadened by an appropriate energy resolution and reported in Figs. 6 and 7), where we noticed that, in the entire Q range of interest, the peak tails on the right-hand side of the spectrum (say, from 35 to 150 meV) are accurately described for both samples by a simple functional form $A \exp(-B\omega - C\omega^2 - D\omega^3)$ with A, B, C, and D as parameters. Thus, we

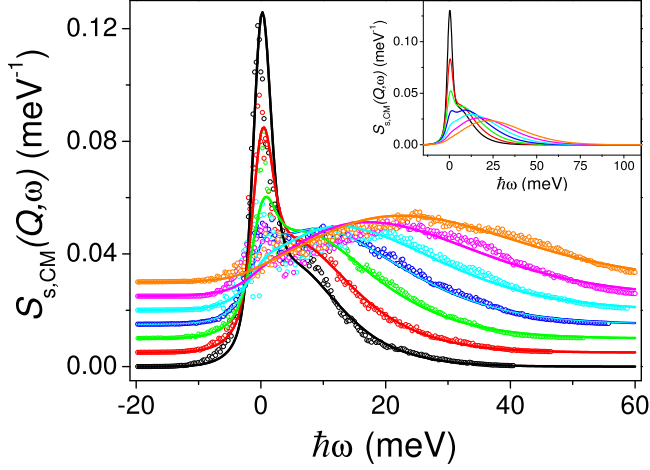FIG. 7. Simulated self-scattering law for H_2 centers of mass in a neon-hydrogen liquid mixture (sample No. 5, $c[H_2] = 3.4\%$, $T = 30.08$ K) from centroid molecular dynamics data via the Gaussian approximation. Reported spectra range from $Q = 2.25$ Å^{-1} (lowest black line) to $Q = 5.25$ Å^{-1} (upmost orange line) with a 0.5-Å^{-1} step. Experimental data from Fig. 3 have been also plotted for comparison. Curves have been vertically shifted for graphic reasons. In the inset, same simulated data have been reported in a wider energy transfer range (no shift applied).
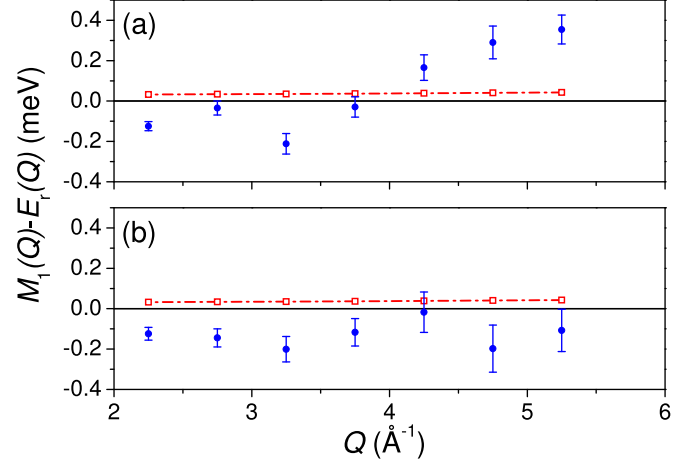

FIG. 8. Deviations of the first spectral moment from recoil energy: experimental data are reported as full blue circles with error bars, while simulated data are shown as empty red squares plus a dashed-dotted line (which is only a guide for the eyes). (a) Contains data for sample No. 4, while (b) for sample No. 5. It is worth noting that error bars represent only the statistical component of data uncertainties.

have used this functional model to fit the experimental data and, subsequently, to extrapolate them to high ω values in order to evaluate the moments needed for our data analysis procedure.

After this procedure, we were able to calculate the first moments of the mentioned experimental spectra and compare them with the theoretical predictions based on the first moment incoherent sum rule [5]:

$$M_1(Q) = \int_{-\infty}^{\infty} d(\hbar\omega) S_{s,\text{CM}}(Q,\omega)\hbar\omega = \frac{\hbar^2 Q^2}{2m_{\text{CM}}}, \quad (7)$$

where the last term is also known as *recoil energy* $E_r(Q)$. So, it is convenient to evaluate the deviations of the numerical estimates of the first spectral moments from the corresponding recoil energy values. Results are reported in Fig. 8, where analogous quantities obtained replacing the experimental $S_{s,\text{CM}}(Q,\omega)$ with the simulated $S_{s,\text{CM}}^{(\text{GA})}(Q,\omega)$ have been also plotted in order to assess the effects of the average over Q in each spectral slice, and of the energy resolution broadening being slightly variable with ω, since these two elements are included in both types of spectra. Two things are to be noted: First, averaging over a ΔQ-thick spectral slice centered at Q, there exists an intrinsic overestimate of $M_1(Q)$, which in the case of a uniform Q distribution is of the order of $\hbar^2 \Delta Q^2/(24 m_{\text{CM}}) = 0.0216$ meV (in our data reduction conditions). Second, the error bars reported in Fig. 8 include only the statistical components of data uncertainties, neglecting all the systematic contributions: not only those coming from the average over Q in each spectral slice and from the energy resolution broadening slightly variable with ω, but also the effects of an approximate Ne subtraction (see Appendix A) and, moreover, of the high energy extrapolation. In fact, the first two sources of systematic uncertainties seem

rather modest for all the Q values, as confirmed by the simulation data also plotted in Fig. 8. So, one has to conclude that the other two sources are indeed more relevant, but are still of the same order of magnitude of the statistical uncertainty. Summarizing: If compared to the corresponding recoil energy values $E_r(Q)$, one observes a discrepancy for experimental $M_1(Q)$ values ranging from 0.2% to 2.4% for sample No. 4, and from 0.1% to 2.4% for sample No. 5, which are both thoroughly satisfactory considering the complexity of the data reduction procedure carried out in Sec. III.

Given the positive fulfillment of the first moment sum rule by our experimental spectra, we decided to further exploit this approach studying the second moment sum rule and its link with the CM mean kinetic energy [5]:

$$\tilde{M}_2(Q) = \int_{-\infty}^{\infty} d(\hbar\omega) S_{s,\text{CM}}(Q,\omega)[\hbar\omega - E_r(Q)]^2$$
$$= \frac{2\hbar^2 Q^2}{3m_{\text{CM}}}\langle E_k \rangle_{\text{CM}}, \quad (8)$$

where $\tilde{M}_2(Q)$ is known as the *second central moment*, i.e., the second moment about the spectral mean $E_r(Q)$. However, differently from the case of an odd moment like in Eq. (7), for the second central moment the instrumental resolution plays some role and has to be accounted for in an effective way through a Q-dependent quantity $\bar{V}_{\text{res}}(Q)$, which is to be subtracted from $\tilde{M}_2(Q)$. A simple way to estimate $\bar{V}_{\text{res}}(Q)$ is the following:

$$\bar{V}_{\text{res}}(Q) \approx \frac{\hbar^2}{8\ln 2}[\Delta\omega(\epsilon)]^2_{\epsilon = E_r(Q)/\hbar}, \quad (9)$$

that is the variance of the instrumental resolution evaluated at the peak mean, i.e., at the recoil energy value. Thus, in this case it is convenient to directly calculate the following
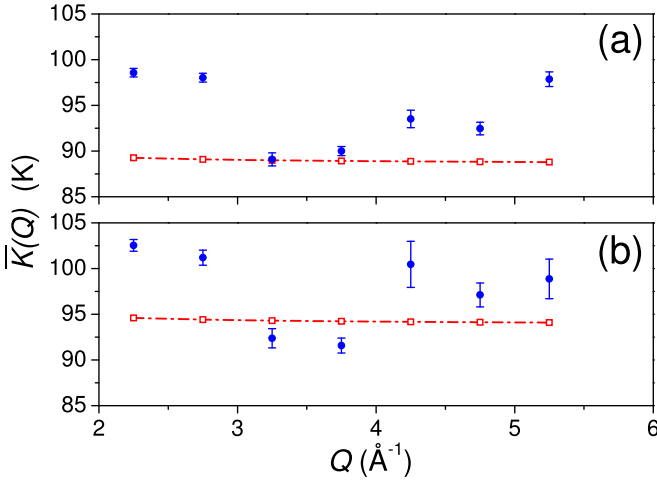
FIG. 9. Mean kinetic energy of the H_2 center of mass from the second central moment of the spectra: experimental data are reported as full blue circles with error bars, while simulated data are shown as empty red squares plus a dashed-dotted line (which is only a guide for the eyes). (a) Contains data for sample No. 4, while (b) for sample No. 5. It is worth noting that error bars represent only the statistical component of the data uncertainties.

empirical function $\bar{K}(Q)$:

$$\bar{K}(Q) = \frac{3m_{CM}}{2\hbar^2 Q^2}(\tilde{M}_2(Q) - \bar{V}_{res}(Q)). \qquad (10)$$

Results are reported in Fig. 9, where the analogous quantities obtained replacing the experimental $S_{s,CM}(Q, \omega)$ with the simulated $S_{s,CM}^{(GA)}(Q, \omega)$ have been also plotted as we did in Fig. 8. The experimental estimates of the CM mean kinetic energies, derived from a fitting procedure on $\bar{K}(Q)$, turned out to be (95 ± 2) K for sample No. 4 and (98 ± 2) K sample No. 5, while the same approach used on simulated spectra provided the following results: (88.84 ± 0.03) K for sample No. 4 and (94.15 ± 0.04) K for sample No. 5. These two pairs of values have to be contrasted to the quantum simulated estimates of $\langle E_k \rangle_{CM}$, which can be simply derived by interpolating data reported in Table II. Considering the experimental uncertainty on $c[H_2]$, one finds (87.4 ± 0.7) K for sample No. 4 and (92.6 ± 0.3) K sample No. 5 making use of the $\langle E_k \rangle^{(sp)}$ data column, and (87.8 ± 0.7) K for sample No. 4 and (93.1 ± 0.3) K for sample No. 5 making use of the $\langle E_k \rangle^{(po)}$ data column.

The first remark to be made concerns the comparison between simulated-data mean kinetic energies and $\langle E_k \rangle^{(sp)}$, which in principle should coincide since both sets are derived from the same CMD $f_{CM}(\omega)$ spectra. On the contrary, one observes a minute overestimate in the values of the former, probably due to the average over Q in each spectral slice and to the energy resolution broadening being slightly variable with ω. This small disagreement sets the intrinsic accuracy of the present $\tilde{M}_2(Q)$ method that can be assumed to be in the interval 1.5%–1.8%. This range is actually very close to the uncertainties of the experimental-data mean kinetic energies (i.e., 1.7%–1.9%) resulting from the fitting procedure, giving rise to an overall uncertainty of about 2.4%. Such a figure can be considered as quite reasonable if compared to equivalent

$\langle E_k \rangle$ results extracted through other techniques like, e.g., *deep inelastic neutron scattering* [41]. However, it is fair to mention that the present $\tilde{M}_2(Q)$ method relies heavily on the high energy extrapolation of some spectral slices, which in the worst case (i.e., at the highest-Q values) contributes to $\tilde{M}_2(Q)$ for about 25%–30% of its total amount. For this reason, we are convinced that the experimental estimates of the CM mean kinetic energies, although 5%–8% higher than the corresponding quantum simulation values, are to be considered as a positive result of the present neutron scattering study. In addition, it is worthwhile to point out that a slightly more satisfactory agreement between experiment and simulations could be obtained making use of a Lennard-Jones potential for the Ne-Ne interaction, as explained in Appendix B.

In principle, it is possible to compare simulation results concerning the mean Laplacian of the system potential energy with the third central moment of the center-of-mass self-scattering law. This is generally done using the so-called Einstein frequency [5] Ω_E. So, on the simulation side one writes [40]

$$\Omega_E^2 = \int_0^\infty f_{CM}(\omega)\omega^2 d\omega, \qquad (11)$$

while experimentally one has to evaluate [6]

$$\tilde{M}_3(Q) = \frac{\hbar^4 Q^2}{2m_{CM}}\Omega_E^2$$

$$= \int_{-\infty}^\infty d(\hbar\omega)S_{s,CM}(Q, \omega)[\hbar\omega - E_r(Q)]^3. \qquad (12)$$

As for Eq. (11), there is no problem to apply it to our CMD data, obtaining the following $\hbar\Omega_E$ estimates: (10.30 ± 0.01) and (11.00 ± 0.02) meV for samples 4 and 5, respectively. However, for Eq. (12) we had to face the same type of problems we experienced in the mean kinetic energy evaluation, but much more severe due to the higher moment degree. In particular, the extrapolation of the high-Q spectral peaks plays an even larger role. For example, already at $Q \approx 4$ Å^{-1}, roughly 50% of the integral above is due to the extrapolated peak tail. In spite of these difficulties (and further issues related to statistical uncertainties), we have attempted the calculation of the third central moments of our experimental spectra using only four data points in the Q range 2.25 Å$^{-1} \leqslant Q \leqslant 3.75$ Å^{-1}, working out the following results for $\hbar\Omega_E$: (10.5 ± 0.3) and (11.0 ± 0.3) meV for samples 4 and 5, respectively. Also, in this case the agreement between experimental and simulated estimates is remarkable.

The next physical information which may be extracted from our experimental spectra is related to the diffusional behavior of the H_2 CMs in the two liquid mixture samples. This task can be accomplished by studying the lowest-Q-value data sets, namely, from $Q = 2.25$ Å^{-1} to $Q = 3.75$ Å^{-1}, where incoherent neutron scattering probes spatial scales large enough to highlight the diffusion process. However, it is very important to stress that MARI (especially before the recent upgrade) was not a spectrometer designed to perform quasielastic neutron scattering measurements since neither its Q and ω ranges, nor the corresponding instrumental resolutions ΔQ and $\Delta \omega$, were optimized to accomplish such experiments. For this reason, this study will provide only a coarse estimate of
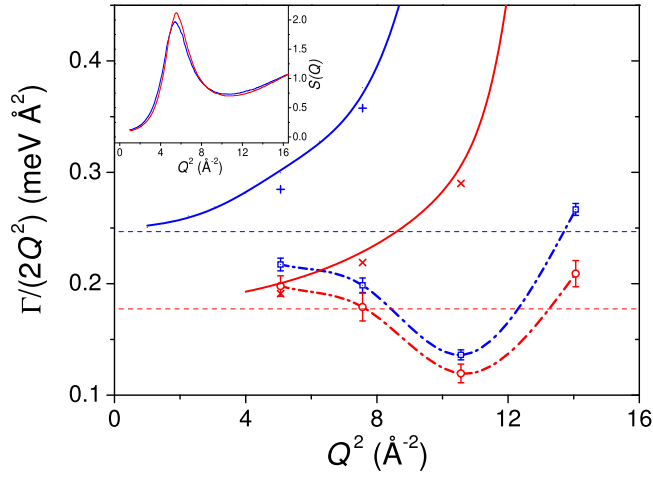
FIG. 10. Ratios between the spectral full width at half maximum, Γ, and $2Q^2$ as a function of Q^2 for sample No. (4) (blue line and plus signs) and sample No. (5) (red line and crosses). Full lines represent the GA-simulated results at the exact Q values reported. Symbols show the same physical quantities, but averaged over Q slices prepared like the experimental data (see main text for details). Experimental data are plotted as empty squares and empty circles for sample No. (4) and No. (5), respectively (while dash-dotted lines are only guides for the eyes). Thin dashed lines exhibit the hydrodynamic limit values, $D_{s,\mathrm{CM}}$, derived from Table II. In the inset, the total static structure factors, $S(Q)$ (see main text for details), for sample No. (4) (blue) and sample No. (5) (red) have been plotted as a function of Q^2.

the self-diffusion coefficients since the mentioned Q range is normally described as that of *space-dependent self-diffusion* [42], where a complete and detailed theory for quantum and semiquantum fluids does not exist yet. Given this scenario, we will focus only on one single spectral feature, namely, the full width at half maximum (FWHM) $\Gamma(Q)$, of the quasielastic peak. So, the selected $S_{s,\mathrm{CM}}(Q, \omega)$ spectra have been fitted by a heuristic multi-Voigtian model (up to four independent Voigt function peaks) which has been analytically deconvoluted for the effect of the instrumental energy resolution. The need to use more than a single Voigtian profile was clearly justified both by the presence of some inelastic features (unrelated to the diffusion process and dealt with in detail below) and by the strong spectral asymmetry induced by the detailed balance. In the case of the present procedure, both the angular and the ω dependencies of $\Delta\omega$ have been carefully taken into account. Subsequently, the resolution-free fitted data have been symmetrized with respect to $\omega = 0$, in order to counter the detailed balance effect, and the experimental FWHM values $\Gamma_{ex}(Q)$ have been determined. A comparison between experimental FWHM results and analogous data worked out from GA-based calculations is particularly important in the case of self-diffusion since the long-time hydrodynamic limit of the GA implies the so-called *continuous diffusion*, while, as mentioned in the Introduction, there are some clues that the H_2 self-dynamics in heavier low-temperature liquids could exhibit jump diffusion features, which are actually incompatible with the GA [43]. Experimental and GA-simulated FWHM results for both mixture samples are plotted in Fig. 10

as ratios $\Gamma/(2Q^2)$, together with the hydrodynamic limit values $D_{s,\mathrm{CM}}$ obtained from Table II through interpolation: $3.75(4) \times 10^{-5}$ cm^2 s^{-1} and $2.70(4) \times 10^{-5}$ cm^2 s^{-1} for samplea No. 4 and No. 5, respectively (reported errors are derived only from CMD statistical uncertainties and so they do not include the additional experimental $c[H_2]$ uncertainties).

An interpretation of the GA behavior is quite straightforward: simulated data show the correct hydrodynamic limit at low-Q values, while, for larger momentum transfers, they exhibit a broadening which grows faster than Q^2. This seems to hold approximately in the same way for both H_2 concentrations. It is a known property of the GA and has been clearly described in the scientific literature [44], where it is shown that, at least up to σQ equal to about 15 (with σ being the Lennard-Jones distance parameter), an overquadratic growth of peak FWHM takes place. Since Ne and H_2 have similar σ values (i.e., 2.79 and 2.94 Å, respectively), this limit can be easily estimated as $Q \approx 5.2$ Å^{-1} (i.e., $Q^2 \approx 27$ Å^{-2}), which, although out of the present FWHM range, seems compatible with our findings about the GA spectra. In Fig. 10 we have reported both single-Q GA widths and analogous quantities averaged over the Q slices used to deal with experimental data: it turns out that averaging has little effect on the extraction of the peak diffusional broadening in GA-simulated data.

As for the experimental data, results are slightly more difficult to be interpreted, even though their general trend looks understandable: the FWHM grows in an underquadratic way (i.e., FWHM/Q^2 falls) for 2.25 Å^{-1} < Q < 3.5 Å^{-1} and then, for higher-Q values, this trend seems reversed with the experimental peak width proceeding parallel to the GA-simulated one. This is in good agreement with the crossover value $\sigma Q \approx 11$, as in Ref. [44]. However, some features are more puzzling: data for the two mixture samples show a strikingly similar behavior, but their separation is lower than expected (i.e., about one third) if one considers the respective hydrodynamic limits. In other words, the widths at the minimum Q value do not seem to approach the CMD-simulated $D_{s,\mathrm{CM}}$, especially the FWHM for sample No. 5 data, which appears definitely too intense at $Q = 2.25$ Å^{-1}. In addition, and probably more important, the minimum value of FWHM/Q^2 is located for both samples at $Q = 3.25$ Å^{-1}, which is larger than the first maximum (i.e., $Q \approx 2.3$ Å^{-1}) of the total static structure factor $S(Q)$ (which has been plotted in the inset of Fig. 10 as a linear combination of all the partial components weighted by the appropriate concentrations). This shift in Q is unexpected since the correspondence between the minimum of FWHM/Q^2 and the first maximum of $S(Q)$ is well established in various simple liquids (Ar, Na, etc.) both experimentally and through simulation work [42,44]. In addition, Wahnström and Sjögren [45] have managed to theoretically reproduce these findings in a reasonably good way using a mode coupling approach. However, it does not look straightforward to generalize their method to binary mixtures exhibiting relevant quantum effects like in our case. Although at the moment we do not have a clear physical explanation of this Q shift, we are confident about its authenticity since, after working on equivalent data taken from a recent H_2-D_2 neutron scattering study (see Fig. 9 in
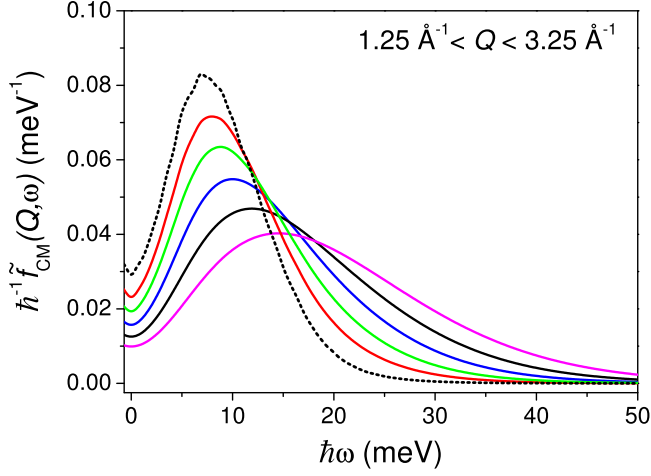
FIG. 11. Simulated pseudospectral function $\tilde{f}_{CM}(Q, \omega)$ for H_2 centers of mass in a neon-hydrogen liquid mixture (sample No. (4), $c[H_2] = 10\%$, $T = 30.1$ K) from centroid molecular dynamics data via Gaussian approximation. Reported spectra range from $Q = 1.25$ Å^{-1} (upmost full red line) to $Q = 3.25$ Å^{-1} (lowest full magenta line) with a 0.5 Å^{-1} step. The exact spectral function $f_{CM}(\omega)$, still from centroid molecular dynamics data, has been also plotted (dotted line).

FIG. 12. Experimental pseudospectral functions $\tilde{f}_{CM}(Q, \omega)$ for H_2 centers of mass in neon-hydrogen liquid mixtures [sample No. (4) in panel (a), sample No. (5) in panel (b)]. Spectra are plotted for $Q = 2.25$ Å^{-1}, $Q = 2.75$ Å^{-1}, and $Q = 3.25$ Å^{-1} (from top to bottom at $\hbar\omega \approx 10$ meV, red, black and blue histograms with error bars, respectively). The $Q \to 0$ extrapolation (see main text for details) of the experimental data above is also reported as a full green line. Finally, the spectral function $f_{CM}(\omega)$, derived from centroid molecular dynamics, has been plotted (dashed black line) after introducing an appropriate instrumentlike frequency broadening.

Ref. [12]), we have found some clues of a similar behavior also there (despite the narrower Q range available). Surely, as we have already mentioned above, these results, although interesting, cannot be considered as conclusive since they are not derived from a proper quasielastic experiment, and so they have neither the optimal (Q, ω) range, nor the binning, nor the resolution. However, as for the departure of the microscopic self-dynamics from the GA in the present neon-hydrogen mixtures, the findings plotted in Fig. 10 can be regarded as a strong clue.

The last point to be dealt with concerning the experimental results is the extraction of the spectral function $f_{CM}(\omega)$ defined in Sec. IV and related to the Kubo transform of the VACF. A very general procedure for the extraction of the VACF spectrum can be expressed by the two following formulas:

$$f_{CM}(\omega) = \lim_{Q \to 0} \tilde{f}_{CM}(Q, \omega);$$

$$\tilde{f}_{CM}(Q, \omega) = \left\{ \frac{4m_{CM}}{Q^2} \frac{\omega^2 + D_{s,CM}^2 Q^4}{\omega} \left[\coth\left(\frac{\hbar\omega}{2k_B T}\right) + 1 \right] \right\}^{-1}$$

$$\times S_{s,CM}(Q, \omega) \Big\}, \quad (13)$$

which slightly modify the Morkel-Verkerk approach [46] in order to correctly take into account the quantum effects via the Bose factor $n(\omega, T) = 1/[\exp(\hbar\omega/k_B T) - 1]$, in close analogy with the relationship between the density of phonon states and the self-scattering law in the case of low temperature solids [5]. A practical test of the validity of Eqs. (13) is reported in Fig. 11 for simulated data related to sample No. 4: $f_{CM}(\omega)$ is directly obtained from CMD as explained in Sec. IV, while the various pseudospectral functions $\tilde{f}_{CM}(Q, \omega)$ have been worked
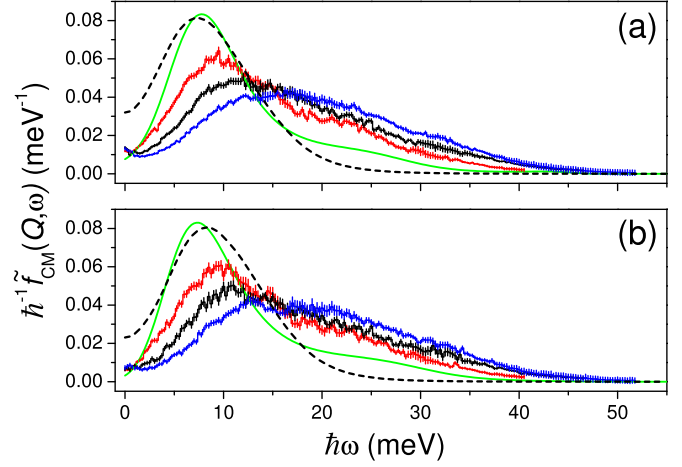
through the aforementioned GA calculations, plotted in Fig. 6, but without including any instrumental resolution broadening. As the Q value reduces, the pseudospectral functions $\tilde{f}_{CM}(Q, \omega)$ smoothly approach the original VACF spectrum $f_{CM}(\omega)$, even in the low ω range which is generally the most critical in this sort of scaling procedure. This positive result is surely expected since it is straightforward to show that the Morkel-Verkerk formulas, although far more general, can be also derived as the low-Q limit from the GA formula itself. To put it in another way, as shown in Fig. 11 by a practical example, GA also complies with Eq. (13), but the latter is much more general than the former.

The previous formulas are not strictly applicable in our case since the present experimental spectra exhibit neither the sufficient statistical accuracy nor the appropriate extension of the low-Q range so to allow a direct extrapolation for $Q \to 0$. Nonetheless, if one tries to perform the $f_{CM}(\omega)$ extraction from the neutron scattering data plotted in Figs. 2 and 3, the pseudospectral functions represented in Fig. 12 are obtained. Subsequently, a simple and rather heuristic extrapolation scheme was devised: for each Q value, the following logarithmic quantity $\ln(\hbar^{-1} \tilde{f}_{CM}(Q, \omega) \times 1.00$ meV) was polynomially fitted obtaining eight Q-dependent coefficients $C_{0-7}(Q)$. These coefficient sets were extrapolated to $Q \to 0$ using a quadratic fitting procedure, giving rise to $C_{0-7}(0)$, which, in turn, were finally exponentiated and normalized to unity in order to work out the best experimental estimate of $f_{CM}(\omega)$. As we have already pointed out, the two extrapolated $f_{CM}(\omega)$ spectra have to be considered only as tentative results; however, looking at Fig. 12, one sees that the agreement with the corresponding CMD data is already at a semiquantitative level, especially dealing with sample No. 4, while sample

No. 5 shows a certain frequency shift of the order of 2–3 meV to the left. Surely, if a detailed observation is carried out, two areas of particular discrepancy can be noted: first, in the low frequency zone (below 5–7 meV) the extrapolated data heavily underestimate the spectral intensity and, consequently, cross the $\omega = 0$ axis at very low values of $f_{CM}(0)$, which entail rather small and unphysical values of the CM self-diffusion coefficients. Second, a hump between 20 and 30 meV is clearly detected in the extrapolated $f_{CM}(\omega)$ for both samples, but is completely missing in the simulated spectra.

VI. CONCLUSIONS

In conclusion, in this work we have measured the neutron scattering spectra of hydrogen mixed with liquid neon (at $T = 30.1$ K) for two values of H_2 molar concentration (namely, 3.4% and 10%), making use of the neutron spectrometer MARI [13]. The two double-differential neutron scattering cross sections aimed to provide a direct access to the self-part of the dynamic structure factor for the H_2 centers of mass in the mentioned liquid samples. In order to accomplish this task, neutron scattering data have been corrected for the standard experimental effects, and, after the subtraction of appropriate neon components, have been studied in the framework of the so-called generalized Young and Koppel model [22–24] for removing the contributions coming from the rotovibrational molecular dynamics. After performing this procedure, one has approximately obtained a mapping of the H_2 center-of-mass self-dynamic structure factor in the momentum transfer interval 2.25 Å$^{-1} < Q < 5.25$ Å^{-1} and in the energy transfer interval -20 meV $< \hbar\omega < 60$ meV, with an average energy resolution (full width at half maximum) ranging in the 2–2.5 meV interval. Subsequently, the quality of these spectral data has been checked exploiting the first incoherent sum rule [5] and found globally satisfactory. Then, their quasielastic parts measured at low momentum transfer (i.e., $Q \leqslant 3.75$ Å^{-1}) have been studied in order to extract information of the H_2 diffusional motion, in spite of the fact that MARI is not an instrument devoted to quasielastic neutron scattering studies. However, after simple symmetrization and deconvolution procedures, we managed to determine the basic spectral feature, namely, the intrinsic peak width, which is Q dependent and related to the H_2 diffusion. These width values turned out to be in a fair agreement with the self-diffusion coefficients simulated via quantum calculations, but also exhibited a peculiar nonmonotonic variation as a function of the momentum transfer which seems compatible with what has been observed in other simple liquids [44] and, in any case, cannot be described by the well-known Gaussian approximation [6]. Although this result is quite remarkable since non-Gaussian effects turned out to be strong, at the present stage no final conclusion on this subject can be drawn given the limitation imposed by the use of the MARI spectrometer, in terms of both Q range and energy transfer resolution. In addition, from the first and the second moments of the processed data, the mean kinetic energy of the H_2 centers of mass has been estimated making use of the mentioned incoherent sum rules and then compared with accurate quantum calculation results. The agreement was found to be reasonably good, even

though (for intrinsic instrumental kinematic reasons) some experimental neutron spectra were not complete and had to be extrapolated via a heuristic fitting procedure in order to evaluate their requested spectral moments.

The cited quantum calculations, obtained via the so-called centroid molecular dynamics [27], provided, as in the case of H_2-D_2 mixtures [4], accurate estimates of the velocity autocorrelation function for the H_2 centers of mass, as well as for the Ne atoms. The former functions appear almost solidlike since their spectra exhibit a clear and strong maximum at frequency values larger than zero and then slowly decrease with a long tail, while the latter ones show the typical almost monotonic diluted-fluid behavior with the spectral maximum being very weak or even absent. These simulated physical quantities, in conjunction with the Gaussian approximation [6], were used to calculate the H_2 center-of-mass self-dynamic structure factor in the same (Q, ω) range as the experimental mapping and at identical thermodynamic conditions. The agreement between neutron measured and calculated spectra turned out to be qualitatively good, even though various discrepancies were clearly detectable, not much differently from the cases of pure H_2 and H_2-D_2, where in the range 1.8 Å$^{-1} < Q < 3.2$ Å^{-1} unquestionable departures from the Gaussian approximation appear. These findings reinforce the conclusions of our previous works [3,4,9,12] on various semiquantum fluids suggesting the need to go beyond the Gaussian approximation for accurately describing the microscopic single-particle dynamics in these systems. In particular, the two liquid mixtures presently studied exhibit relevant non-Gaussian effects surely similar, but even more intense than those revealed in the other fluids mentioned, confirming our original idea about the positive connection between caging effects due to heavy atoms (i.e., Ne) surrounding diluted lightweight impurities (i.e., H_2) and the breakdown of the Gaussian approximation. However, we have to honestly admit that our results on H_2 in Ne are slightly less compelling than the previous ones on H_2 and H_2-D_2 because of some experimental uncertainties related both to the statistical accuracy of the measurements and, moreover, to the subtraction of the scattering signal due to the neon presence. Thus, even though this study greatly improves the quality of the available neutron spectra [9,12,47] of H_2 impurities in liquid Ne, in terms of energy resolution, data analysis, and constant-Q cuts, further experimental effort is surely desirable on this system as well as on analogous H_2 mixtures with liquid argon [47]. In addition, it is also heartily recommended that detailed quasielastic neutron scattering studies on the H_2 motion in various simple liquids (such as D_2, Ne, and Ar) are performed in order to clarify the nature of the diffusion mechanism (e.g., its differences from the Gaussian approximation and the hydrodynamic Fick regime).

<center>**APPENDIX A**</center>

Neutron scattering from a simple-liquid binary mixture (formed by type-"1" and type-"2" atoms) can be described in various ways, the simplest of which is probably the Faber-Ziman approach [48], where one introduces the partial components of the so-called distinct dynamic structure factor $S_{d,\alpha\text{-}\beta}(Q,\omega)$ (with α and β equal to 1 or 2), as well as of the self-dynamic structure factor $S_{s,\alpha}(Q,\omega)$ (with α equal to 1 or 2). In this case, the double-differential scattering cross section, including both coherent and incoherent signal, reads as

$$\left(\frac{d^2\sigma}{d\Omega\,dE'}\right)_{1+2} = \frac{k'}{k}\left[c_1^2(\bar{b}_1)^2 S_{d,1\text{-}1}(Q,\omega) + c_2^2(\bar{b}_2)^2 S_{d,2\text{-}2}(Q,\omega) + 2c_1c_2\,\bar{b}_1\bar{b}_2\,S_{d,1\text{-}2}(Q,\omega)\right.$$
$$\left. + c_1\left(\frac{\sigma_{t,1}}{4\pi}\right)S_{s,1}(Q,\omega) + c_2\left(\frac{\sigma_{t,2}}{4\pi}\right)S_{s,2}(Q,\omega)\right], \tag{A1}$$

where (k'/k) is the well-known kinematic factor [5], c_α are the concentrations of the two species, $\bar{b}_\alpha$ are their coherent scattering lengths, and $\sigma_{t,\alpha}$ their total (coherent plus incoherent) cross sections. Needless to say, in case of a pure liquid, for example "1," $c_1 = 1$ and $c_2 = 0$, so that the previous expression reduces to the standard formula for inelastic neutron scattering:

$$\left(\frac{d^2\sigma}{d\Omega\,dE'}\right)_1 = \frac{k'}{k}\left[(\bar{b}_1)^2\,S_{d,1\text{-}1}(Q,\omega) + \left(\frac{\sigma_{t,1}}{4\pi}\right)S_{s,1}(Q,\omega)\right] = \frac{k'}{k}\left[(\bar{b}_1)^2\,S_1(Q,\omega) + \left(\frac{\sigma_{\text{inc},1}}{4\pi}\right)S_{s,1}(Q,\omega)\right], \tag{A2}$$

where the dynamic structure factor $S_1(Q,\omega)$ is simply given by $S_{d,1\text{-}1}(Q,\omega) + S_{s,1}(Q,\omega)$. In our case, Eqs. (A1) and (A2) have to be slightly modified to take into account that one type of molecule, namely H_2, is not monatomic, but, on the contrary, exhibits a diatomic structure and so additional rotovibrational excitations have to be included in the scattering law. It can be shown [23,24] that, in the case of pure hydrogen, Eq. (A2) can be cast in the following form (if the high-energy H_2 vibrational excitations can be neglected), where j and j' are the initial and final rotational quantum numbers, respectively:

$$\left(\frac{d^2\sigma}{d\Omega\,dE'}\right)_{H_2} = \frac{k'}{k}\left[u(Q)\,S_{d,\text{CM-CM}}(Q,\omega) + \sum_{j,j'}a(Q;j,j')\,S_{s,\text{CM}}(Q,\omega)\otimes\delta(\hbar\omega - E_{j,j'})\right], \tag{A3}$$

with $u(Q)$ replacing the squared coherent scattering length, $S_{d,\text{CM-CM}}(Q,\omega)$ being the distinct dynamic structure factor of the H_2 CM, $S_{s,\text{CM}}(Q,\omega)$ being the self-dynamic structure factor of the H_2 CM, $a(Q;j,j')$ controlling the intensity of the rotational transition under consideration, and $E_{j,j'}$ being the energy shift due to this rotational transition. The $u(Q)$ term is given by

$$u(Q) = 4(\bar{b}_H)^2\exp[-2W_v(Q)]\,j_0^2(Qd_H/2), \tag{A4}$$

where $\exp[-2W_v(Q)]$ is the tiny internal vibrational Debye-Waller factor, while $j_0(x)$ is the zeroth order spherical Bessel function of the first kind, and d_H is the mean interatomic distance of H_2. Leaving aside $a(Q;j,j')$, which is clearly defined in the mentioned literature, it is straightforward to generalize Eqs. (A1) and (A3) to our H_2-containing hydrogen mixture (with "1"= Ne and "2"= CM):

$$\left(\frac{d^2\sigma}{d\Omega\,dE'}\right)_{\text{mix}} = \frac{k'}{k}\left[c[\text{Ne}]^2(\bar{b}_{\text{Ne}})^2\,S_{d,\text{Ne-Ne}}(Q,\omega) + c[\text{H}_2]^2\,u(Q)\,S_{d,\text{CM-CM}}(Q,\omega)\right.$$

$$+ 4c[\text{Ne}]c[\text{H}_2]\bar{b}_{\text{Ne}}\bar{b}_H e^{-W_v(Q)}j_0(Qd_H/2)S_{d,\text{Ne-CM}}(Q,\omega) + c[\text{Ne}]\left(\frac{\sigma_t[\text{Ne}]}{4\pi}\right)S_{s,\text{Ne}}(Q,\omega)$$

$$\left. + c[\text{H}_2]\sum_{j,j'}a(Q;j,j')S_{s,\text{CM}}(Q,\omega)\otimes\delta(\hbar\omega - E_{j,j'})\right], \tag{A5}$$

where the so-called "cross" dynamic structure factor $S_{d,\text{Ne-CM}}(Q,\omega)$ has been introduced. It describes the spectrum of the time-dependent correlation between Ne atoms and CMs of the H_2 molecules in the mixture. Since $c[\text{H}_2]$ is in our case rather modest (not larger than 10%) and the Ne incoherent cross section is thoroughly negligible [20], it is possible to simplify Eq. (A5) giving rise to an easier and slightly approximate form

$$\left(\frac{d^2\sigma}{d\Omega\,dE'}\right)_{\text{mix}} \simeq \frac{k'}{k}\left[c[\text{Ne}]^2\left(\frac{\sigma_t[\text{Ne}]}{4\pi}\right)S_{\text{Ne}}(Q,\omega) + 4c[\text{Ne}]c[\text{H}_2]\bar{b}_{\text{Ne}}\bar{b}_H e^{-W_v(Q)}j_0(Qd_H/2)\right.$$

$$\times S_{d,\text{Ne-CM}}(Q,\omega) + (c[\text{Ne}] - c[\text{Ne}]^2)\left(\frac{\sigma_t[\text{Ne}]}{4\pi}\right)S_{s,\text{Ne}}(Q,\omega)$$

$$\left. + c[\text{H}_2]\sum_{j,j'}a(Q;j,j')S_{s,\text{CM}}(Q,\omega)\otimes\delta(\hbar\omega - E_{j,j'})\right]. \tag{A6}$$

It is worth commenting the third term in the formula above: it is the so-called "diffuse" scattering component, typical of the Faber-Ziman approach to mixtures, and represents a term which is incoherent in its form (being proportional to the self-dynamic structure factor), but purely coherent in its nature (since we have seen that the Ne incoherent cross section is negligible).

Since the final purpose of Sec. III is to isolate the scattering contribution due to the self-dynamics of the H_2 molecules, the strategy of the present approach will be to manipulate the four terms in Eq. (A6) in order to leave only the last. Rigorously speaking, this is an impossible task since three dynamic structure factors, namely, $S_{Ne}(Q, \omega)$, $S_{d,Ne\text{-}CM}(Q, \omega)$, and $S_{s,Ne}(Q, \omega)$, are experimentally unknown for the two mixture samples. However, looking at Table I, where temperatures, H_2 impurity concentrations, and total molecular densities are reported, it is possible to assume that, due to the small variations of n, $S_{Ne}(Q, \omega)$ might be considered basically the same in all the three measured samples. In this way, going back to Eq. (A2), one can easily remove the first term in Eq. (A6) by simple subtraction:

$$
c[\mathrm{H_2}]^{-1}\left(\frac{d^2\sigma}{d\Omega\,dE'}\right)_{\mathrm{mix}} - c[\mathrm{H_2}]^{-1}c[\mathrm{Ne}]^2\left(\frac{d^2\sigma}{d\Omega\,dE'}\right)_{\mathrm{Ne}} \simeq \frac{k'}{k}\Bigg[4\,c[\mathrm{Ne}]\,\bar{b}_{\mathrm{Ne}}\,\bar{b}_{\mathrm{H}}\,e^{-W_v(Q)}\,j_0(Qd_{\mathrm{H}}/2)S_{d,\mathrm{Ne\text{-}CM}}(Q, \omega)
$$

$$
+ c[\mathrm{H_2}]^{-1}(c[\mathrm{Ne}] - c[\mathrm{Ne}]^2)\left(\frac{\sigma_t[\mathrm{Ne}]}{4\pi}\right)S_{s,\mathrm{Ne}}(Q, \omega)
$$

$$
+ \sum_{j,j'} a(Q; j, j')S_{s,\mathrm{CM}}(Q, \omega) \otimes \delta(\hbar\omega - E_{j,j'})\Bigg]. \tag{A7}
$$

Together with the hydrogen contribution, the previous equation still exhibits two extra terms: one coherent due to the "cross" scattering between Ne atoms and H_2 molecules, and one representing the self-diffuse scattering from the system. Another strategy could consist in performing a slightly different subtraction (with the weight $c[\mathrm{Ne}]^2$ replaced by $c[\mathrm{Ne}]$) so to obtain

$$
c[\mathrm{H_2}]^{-1}\left(\frac{d^2\sigma}{d\Omega\,dE'}\right)_{\mathrm{mix}} - c[\mathrm{H_2}]^{-1}c[\mathrm{Ne}]\left(\frac{d^2\sigma}{d\Omega\,dE'}\right)_{\mathrm{Ne}} \simeq \frac{k'}{k}\Bigg[4\,c[\mathrm{Ne}]\,\bar{b}_{\mathrm{Ne}}\,\bar{b}_{\mathrm{H}}\,e^{-W_v(Q)}\,j_0(Qd_{\mathrm{H}}/2)S_{d,\mathrm{Ne\text{-}CM}}(Q, \omega)
$$

$$
+ c[\mathrm{H_2}]^{-1}(c[\mathrm{Ne}] - c[\mathrm{Ne}]^2)\left(\frac{\sigma_t[\mathrm{Ne}]}{4\pi}\right)[S_{s,\mathrm{Ne}}(Q, \omega) - S_{\mathrm{Ne}}(Q, \omega)]
$$

$$
+ \sum_{j,j'} a(Q; j, j')S_{s,\mathrm{CM}}(Q, \omega) \otimes \delta(\hbar\omega - E_{j,j'})\Bigg], \tag{A8}
$$

which contains an additional Ne term, but exhibiting a negative sign. Before choosing the better approach, it is crucial to numerically compare the integrated magnitudes of the various unwanted terms with one another and with the hydrogen contribution which will be selected (see Sec. III) for accomplishing further studies, namely, the $j = 1 \rightarrow j' = 1$ transition. Choosing the less favorable case [i.e., sample No. 4] with the higher H_2 concentration $c[\mathrm{H_2}] = 10\%$, one has to calculate the following ω-integrated quantities for Eq. (A7):

$$
f_{\mathrm{Ne\text{-}CM}}(Q) = 4\,c[\mathrm{Ne}]\,\bar{b}_{\mathrm{Ne}}\,\bar{b}_{\mathrm{H}}\,e^{-W_v(Q)}\,j_0(Qd_{\mathrm{H}}/2)S_{\times}(Q)
$$

$$
\simeq -4\,c[\mathrm{Ne}]\left(\frac{\sqrt{\sigma_{\mathrm{coh}}[\mathrm{Ne}]\sigma_{\mathrm{coh}}[\mathrm{H}]}}{4\pi}\right)e^{-W_v(Q)}\,j_0(Qd_{\mathrm{H}}/2)\{[S_{\mathrm{Ne}}(Q)S_{\mathrm{CM}}(Q)]^{1/2} - 1\};
$$

$$
f_{s,\mathrm{Ne}}(Q) = c[\mathrm{H_2}]^{-1}(c[\mathrm{Ne}] - c[\mathrm{Ne}]^2)\left(\frac{\sigma_t[\mathrm{Ne}]}{4\pi}\right);
$$

$$
f_{11,\mathrm{CM}}(Q) = a(Q; 1, 1)
$$

$$
= 4\,x_1\,e^{-2W_v(Q)}\big[j_0^2(Qd_{\mathrm{H}}/2) + 2j_2^2(Qd_{\mathrm{H}}/2)\big]\left[\left(\frac{\sigma_{\mathrm{coh}}[\mathrm{H}]}{4\pi}\right) + \frac{2}{3}\left(\frac{\sigma_{\mathrm{inc}}[\mathrm{H}]}{4\pi}\right)\right], \tag{A9}
$$

where $S_{\times}(Q)$ represents the integral of $S_{d,\mathrm{Ne\text{-}CM}}(Q, \omega)$ over ω, and x_1 is the relative population of the rotational species $j = 1$. Similarly, for Eq. (A8) one writes

$$
g_{\mathrm{Ne\text{-}CM}}(Q) = f_{\mathrm{Ne\text{-}CM}}(Q);
$$

$$
g_{s,\mathrm{Ne}}(Q) = c[\mathrm{H_2}]^{-1}(c[\mathrm{Ne}] - c[\mathrm{Ne}]^2)\left(\frac{\sigma_t[\mathrm{Ne}]}{4\pi}\right)[1 - S_{\mathrm{Ne}}(Q)];
$$

$$
g_{11,\mathrm{CM}}(Q) = f_{11,\mathrm{CM}}(Q). \tag{A10}
$$

Summing all the unwanted contributions in Eq. (A9), $f_{un}(Q) = f_{\mathrm{Ne\text{-}CM}}(Q) + f_{s,\mathrm{Ne}}(Q)$, and those in Eq. (A10), $g_{un}(Q) = g_{\mathrm{Ne\text{-}CM}}(Q) + g_{s,\mathrm{Ne}}(Q)$, we can finally establish a comparison with the $j = 1 \rightarrow j' = 1$ hydrogen term in the whole Q range
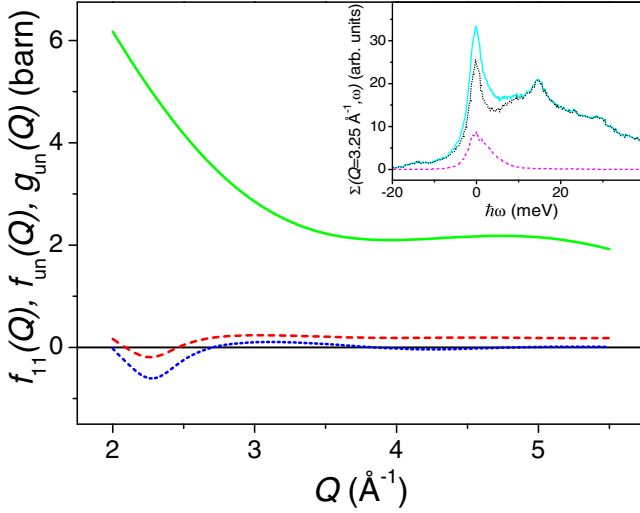
FIG. 13. Simulated scattering contributions (integrated over all the energy transfer range) for sample No. (4) after subtracting the pure neon signal. Full green line stands for $f_{11}(Q)$, the ortho-hydrogen contribution related to the transition $j = 1 \rightarrow j' = 1$, dashed red line represents $f_{un}(Q)$, while dotted blue line $g_{un}(Q)$ (see Appendix A for details). In the inset an example of the Ne signal subtraction for sample No. (4) has been reported ($Q = 3.25$ Å^{-1}): full cyan line represents the signal from the mixture, dashed magenta line that from pure Ne, and dotted black line stands for the difference between the two, related to the n-H$_2$ signal.

of interest (see Fig. 13). These estimates have been calculated using $S_{Ne}(Q)$ and $S_{CM}(Q)$ values obtained from Refs. [49,50]], respectively (after performing the usual corrections for the small molecular density differences). As for the $S_\times(Q)$, a reasonable, although highly heuristic, combination rule for $S_{Ne}(Q)$ and $S_{CM}(Q)$ has been chosen. It is straightforward to see in Fig. 13 that both unwanted contributions are generally much smaller than the selected hydrogen one, although they do not appear to be totally irrelevant, at least for $Q < 3.5$ Å^{-1} where $g_{un}(Q)$ is non-negligible. In fact, it is interesting to note that the absolute value of $g_{un}(Q)$ is much more intense than that of $f_{un}(Q)$ in the low-Q region (say, for $Q < 2.5$ Å^{-1}), while for higher momentum transfer values the trend becomes the opposite. For this reason, in our data reduction procedure we have applied an appropriate (and Q-dependent) linear combination between the two Ne spectra

to be subtracted appearing in Eqs. (A7) and (A8), respectively, setting in this way the resulting unwanted contributions to their lowest possible values.

APPENDIX B

As mentioned in Sec. IV, the molecular model used for our quantum CMD simulations included three pairwise additive potentials, namely, Ne-Ne, Ne-H$_2$ CM, and H$_2$ CM-H$_2$ CM, the first being modeled via a spherically symmetric potential proposed by Aziz and Slaman [28]. Its form is known as HFD-B and contains Gaussian and exponential components at low values of the Ne-Ne distance r, van der Waals ones (proportional to r^{-6}, r^{-8}, and r^{-10}) at high distance values, and, finally, an appropriate switching function to suppress the van der Waals part at close distances. This type of interatomic interaction has been successfully used for noble gases in a wide range of applications and compares still quite well with the most modern *ab initio* potentials for Ne and Ar [51], especially if contrasted to the old Lennard-Jones potential schemes. However, concerning Ne, some evidences about the superiority of the Lennard-Jones form (using, e.g., the Morales and Nuevo parametrization [52]) to predict the correct system density in the liquid state (pure and mixed with hydrogen) have been pointed out by Challa and Johnson [30] in the context of accurate PIMC simulations devoted to the study of the excess volume of the mentioned mixture. As a matter of fact, these authors employed a slightly different Aziz Ne-Ne potential, called HFD-C2 [53], rather than the HFD-B one, but, given the strong resemblance between these two Aziz potentials, we felt motivated to check the effect the potential change on our CMD simulation results. To this aim, we have replaced the Aziz HFD-B potential with a standard (i.e., 12-6) Lennard-Jones one exhibiting the following parameters: $\epsilon/k_B = 36.83$ K and $\sigma = 2.79$ Å [52]. Two thermodynamic states have been investigated, actually those in Table II which are closest to the experimental conditions, namely, Nos. iii and vii, using exactly the same conditions as those applied to the calculations described in Sec. IV. A comparison between the obtained CMD computational results (i.e., self-diffusion coefficients and mean kinetic energies) can be found in Table III, where differences larger than the respective statistical uncertainties are reported. In particular, hydrogen dynamics deserves some comments since, quite unexpectedly, it seems the more affected by a potential change concerning

TABLE III. Thermodynamic conditions and computational results concerning the two liquid samples simulated at $T = 30.0$ K making use of two distinct Ne-Ne pairwise potential, namely, Aziz HFD-B [28] (AZ) and Lennard-Jones [52] (LJ). Table includes potential form, total number of particles N, number of H$_2$ molecules $N[H_2]$, hydrogen concentration $c[H_2]$, total molecular density n, self-diffusion coefficient D_s for H$_2$ CM and Ne, mean kinetic energy $\langle E_k \rangle^{(sp)}$ from VACF spectra for H$_2$ CM and Ne, mean kinetic energy $\langle E_k \rangle^{(po)}$ from PIMC "polymers" for H$_2$ CM and Ne. See main text and Appendix B for details.

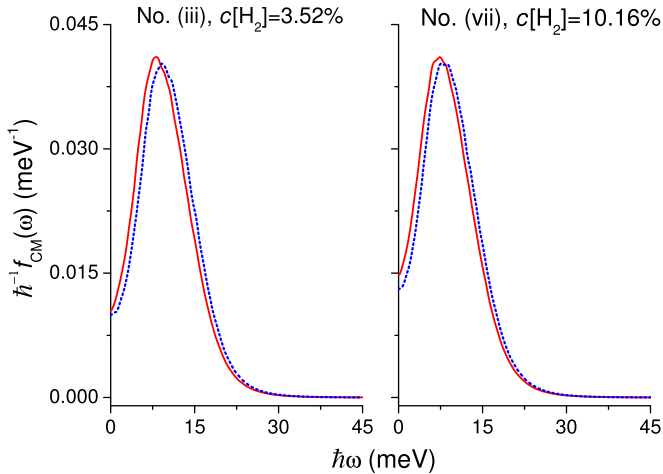| Pot.	N	$N[H_2]$	$c[H_2]$ (%)	n (nm^{-3})	$D_{s,CM}$ (10^{-5} cm^2 s^{-1})	$D_{s,Ne}$ (10^{-5} cm^2 s^{-1})	$\langle E_k \rangle^{(sp)}_{CM}$ (K)	$\langle E_k \rangle^{(sp)}_{Ne}$ (K)	$\langle E_k \rangle^{(po)}_{CM}$ (K)	$\langle E_k \rangle^{(po)}_{Ne}$ (K)
AZ	256	9	3.52	33.07	2.71(4)	2.36(1)	92.6(2)	53.82(1)	93.1(2)	53.69(1)
LJ	256	9	3.52	33.07	2.54(3)	2.32(1)	97.6(3)	53.77(1)	98.3(3)	53.49(5)
AZ	256	26	10.16	30.94	3.78(4)	2.82(1)	87.4(1)	53.15(1)	87.8(1)	53.03(1)
LJ	256	26	10.16	30.94	3.37(1)	2.83(1)	91.6(1)	52.87(1)	92.0(1)	52.63(1)

FIG. 14. Simulated spectral functions $f_{CM}(\omega)$ in two selected neon-hydrogen mixtures reported in Table II, namely, Nos. iii and vii, and in Table III. Data obtained from the Aziz HFD-B Ne-Ne potential [28] are plotted as full red lines, while those from the Lennard-Jones one [52] as dotted blue lines.

the Ne-Ne interaction only. For example, while neon diffusion coefficients are practically unchanged, the hydrogen ones decrease in a sizable way, namely, 6% and 11% for simulated samples No. iii and No. vii, respectively. A similar scenario can be seen if mean kinetic energy estimates (both from VACF spectra and from PIMC "polymers") are taken into account: neon values are almost insensitive to the Ne-Ne potential change, while the H_2 CM ones show an increase of about 5% for both simulated samples.

A more complete picture of this phenomenon can be derived looking at Fig. 14, where the spectral functions $f_{CM}(\omega)$, related to the hydrogen VACFs, have been plotted. Lennard-Jones spectra appear blue-shifted (this explains the larger $\langle E_k \rangle_{CM}$) and, in addition, slightly more solidlike, in agreement with the smaller value of D_s. The physical reason of such an effect of the Ne-Ne potential change is not easy to be conceived since this interaction does not directly affect the

H_2 molecules. One could speculate that the mentioned potential influences the Ne pseudocage surrounding a hydrogen molecule in the liquid, making it more rigid. However, a simple inspection of the Ne-Ne pair correlation functions $g(r)$ (derived, as a by-product, from our quantum simulations) does not completely support this picture since the first $g(r)$ maximum appears more or less at the same position in r and, moreover, the Lennard-Jones potential slightly shifts the base of the main Ne-Ne peak on the right, giving rise to larger, and not narrower, pseudocages.

Moving to the comparison of the new simulated data with our experimental results, one sees in Sec. V, where the fitted $\bar{K}(Q)$ are reported to be (95 ± 2) K for sample No. 4 and (98 ± 2) K for sample No. 5, that the Lennard-Jones $\langle E_k \rangle_{CM}$ values have substantially improved the agreement between CMD and neutron estimates, although for the less diluted sample the increase is not yet completely sufficient. From the Lennard-Jones $f_{CM}(\omega)$ it is possible, exploiting the GA, to reevaluate the self-scattering laws for the H_2 centers of mass plotted in Figs. 4 and 6 (including the instrumental energy transfer resolution) and, subsequently, to compare these spectra with the neutron scattering ones reported in Figs. 2 and 3. For the sake of brevity, this final comparison will be only discussed verbally but not shown in figures. Dealing with the experimental sample No. 4, which corresponds to simulation No. vii in Table II, the agreement is deteriorated for $Q = 2.25$ Å^{-1}, but is improved for 2.75 Å$^{-1} \leqslant Q \leqslant 3.75$ Å^{-1}. At higher-Q values there is no appreciable change with respect to the Aziz-based data. On the other hand, for the experimental sample No. 5, which corresponds to simulation No. iii, the agreement is once again deteriorated for $Q = 2.25$ Å^{-1} data, while elsewhere there is no appreciable change with respect to the Aziz-based data.

In conclusion, there are some clues that the Lennard-Jones Ne-Ne potential is slightly superior than the Aziz one in reproducing the microscopic dynamic features probed by our experiment, although this improvement does not seem to be so relevant to justify a complete recalculation of all the CMD-simulated spectral quantities.

[1] See, for example, K. Hyeon-Deuk and K. Ando, Phys. Chem. Chem. Phys. **18**, 2314 (2016) and references therein.

[2] A. F. Andreev and Yu. A. Kosevich, Zh. Eksp. Teor. Fiz. **77**, 2518 (1979) [Sov. Phys.–JETP **50**, 1218 (1979)].

[3] M. Celli, U. Bafile, D. Colognesi, A. De Francesco, F. Formisano, E. Guarini, M. Neumann, and M. Zoppi, Phys. Rev. B **84**, 140510(R) (2011).

[4] D. Colognesi, U. Bafile, M. Celli, M. Neumann, and A. Orecchini, Phys. Rev. E **92**, 012311 (2015).

[5] S. W. Lovesey, *Theory of Neutron Scattering from Condensed Matter*, Vol. I (Oxford University Press, Oxford, 1987).

[6] A. Rahman, K. S. Singwi, and A. Sjölander, Phys. Rev. **126**, 986 (1962).

[7] K. Sköld, J. M. Rowe, G. Ostrowski, and P. D. Randolph, Phys. Rev. A **6**, 1107 (1972).

[8] D. Colognesi, M. Celli, M. Neumann, and M. Zoppi, Phys. Rev. E **70**, 061202 (2004).

[9] M. Celli, D. Colognesi, M. Zoppi, and A. J. Ramirez-Cuesta, J. Low Temp. Phys. **138**, 887 (2005).

[10] A. M. Dyugaev, J. Low Temp. Phys. **78**, 79 (1990).

[11] D. E. O'Reilly and E. M. Peterson, J. Chem. Phys. **66**, 934 (1977).

[12] M. Celli, D. Colognesi, A. J. Ramirez-Cuesta, and M. Zoppi, Phys. B (Amsterdam) **350**, e1083 (2004).

[13] K. H. Andersen, Nucl. Instrum. Methods Phys. Res., Sect. A **371**, 472 (1996).

[14] V. A. Rabinovich, A. A. Vasserman, V. I. Nedostup, and L. S. Veksler, *Thermophysical Properties of Neon, Argon, Krypton and Xenon*, Vol. 10 (National Reference Data Service, Moscow, 1976).

[15] R. D. McCarty, J. Hord, and H. M. Roder, *Selected Properties of Hydrogen*, NBS Monograph 168 (NBS, Boulder, CO, 1981).

[16] D. Güsewell, F. Schmeissner, and J. Schmid, Cryogenics **11**, 311 (1971).

[17] W. B. Streett, J. Chem. Thermodyn. **5**, 313 (1973).

[18] T. M. Flynn, *Cryogenic Engineering* (Marcel-Dekker, New York, 2005).

[19] C. K. Heck and P. L. Barrick, Liquid-Vapor Phase Equilibria of the Neon-Normal Hydrogen System, in *Advances in Cryogenic Engineering*, Vol. 11, edited by K. D. Timmerhaus (Springer, Boston, 1966).

[20] V. F. Sears, Neutron News **3**, 26 (1992).

[21] W. D. Seiffert, Report No. EUR 4455 d (unpublished); W. D. Seiffert, B. Weckermann, and R. Misenta, Z. Naturforsch. A **25**, 967 (1970).

[22] J. A. Young and J. U. Koppel, Phys. Rev. **135**, A603 (1964).

[23] V. F. Sears, Can. J. Phys. **44**, 1279 (1979).

[24] M. Zoppi, Phys. B (Amsterdam) **183**, 235 (1993).

[25] A. Bickermann, H. Spitzer, H. Stiller, H. Meyer, R. E. Lechner, and F. Volino, Z. Phys. B **31**, 345 (1978).

[26] W. Langel, D. L. Price, R. O. Simmons, and P. E. Sokol, Phys. Rev. B **38**, 11275 (1988).

[27] J. Cao and G. A. Voth, J. Chem. Phys. **100**, 5106 (1994).

[28] R. A. Aziz and M. J. Slaman, Chem. Phys. **130**, 187 (1989).

[29] M. Faubel, F. A. Gianturco, F. Ragnetti, L. Y. Rusin, F. Sondermann, U. Tappe, and J. P. Toennies, J. Chem. Phys. **101**, 8800 (1994).

[30] S. R. Challa and J. K. Johnson, J. Chem. Phys. **111**, 724 (1999).

[31] I. F. Silvera and V. V. Goldman, J. Chem. Phys. **69**, 4209 (1978).

[32] M. H. Müser, Comput. Phys. Commun. **147**, 83 (2002).

[33] W. G. Hoover, *Computational Statistical Mechanics* (Elsevier, Amsterdam, 1991).

[34] W. H. Press, S. Teukolsky, W. T. Vetterling, and B. P. Flannery, *Numerical Recipes in Fortran 90. The Art of Parallel Scientific Computing* (Cambridge University Press, Cambridge, 1996).

[35] R. Kubo, Rep. Prog. Phys. **29**, 255 (1966).

[36] S. Bellissima, M. Neumann, E. Guarini, U. Bafile, and F. Barocchi, Phys. Rev. E **95**, 012108 (2017).

[37] T. F. Miller III and D. E. Manolopoulos, J. Chem. Phys. **122**, 184503 (2005).

[38] K. Singer and W. Smith, Mol. Phys. **64**, 1215 (1988).

[39] M. F. Herman, E. J. Bruskin, and B. J. Berne, J. Chem. Phys. **76**, 5150 (1982).

[40] K. S. Singwi and M. P. Tosi, Phys. Rev. **149**, 70 (1966).

[41] C. Andreani, D. Colognesi, J. Mayers, G. F. Reiter, and R. Senesi, Adv. Phys. **54**, 377 (2005).

[42] J. P. Boon and S. Yip, *Molecular Hydrodynamics* (McGraw-Hill, London, 1982).

[43] M. Bée, *Quasielastic Neutron Scattering* (Hilger, Bristol, 1988).

[44] U. Balucani and M. Zoppi, *Dynamics of the Liquid State* (Clarendon, Oxford, 1994) and references therein.

[45] G. Wahnström and L. Sjögren, J. Phys. C: Solid State Phys. **15**, 401 (1982).

[46] C. Morkel and C. Gronemeyer, Z. Phys. B **72**, 433 (1988); P. Verkerk, Nuovo Cimento Soc. Ital. Fis., D **12**, 441 (1990).

[47] O. J. Eder, S. H. Chen, and P. A. Egelstaff, Proc. Phys. Soc. **89**, 833 (1966).

[48] T. E. Faber and J. M. Ziman, Philos. Mag. **11**, 153 (1965).

[49] L. M. Sesé, Mol. Phys. **89**, 1783 (1996).

[50] J. Dawidowski, F. J. Bermejo, M. L. Ristig, B. Fåk, C. Cabrillo, R. Fernàndez-Perea, K. Kinugawa, and J. Campo, Phys. Rev. B **69**, 014207 (2004); M. Celli, U. Bafile, G. J. Cuello, F. Formisano, R. Magli, E. Guarini, M. Neumann, and M. Zoppi, *ibid.* **71**, 014205 (2005).

[51] A. E. Nasrabad, R. Laghaei, and U. K. Deiters, J. Chem. Phys. **121**, 6423 (2018).

[52] J. J. Morales and M. J. Nuevo, J. Comput. Chem. **16**, 105 (1995).

[53] R. A. Aziz, in *Inert Gases*, edited by M. L. Klein (Springer, Berlin, 1984).